Petroleum Science 23 (2026) 1929–1954

Contents lists available at ScienceDirect

Petroleum Science

journal homepage: www.keaipublishing.com/en/journals/petroleum-science

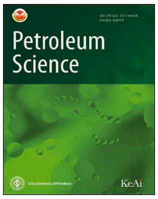

Original Paper

Structural-state integrated modeling of multi-mechanism formation damage during drilling–completion

Ke-Ming Sheng [a,c,d], Guan-Cheng Jiang [b,c,e,*], Ming-Liang Du [b,c], Lan Qiao [f], Yin-Bo He [b,c]

[a] *College of Artificial Intelligence, China University of Petroleum (Beijing), Beijing, 102249, China*
[b] *College of Petroleum Engineering, China University of Petroleum (Beijing), Beijing, 102249, China*
[c] *MOE Key Laboratory of Petroleum Engineering, China University of Petroleum (Beijing), Beijing, 102249, China*
[d] *School of Science & Engineering, University of Dundee, Dundee DD1 4HN, United Kingdom*
[e] *National Engineering Research Center of Oil & Gas Drilling and Completion Technology, Beijing, 102249, China*
[f] *College of Chemical Engineering and Environment, China University of Petroleum (Beijing), Beijing, 102249, China*

ARTICLE INFO

Article history:
Received 5 September 2025
Received in revised form
6 January 2026
Accepted 6 January 2026
Available online 12 January 2026

Edited by Jia-Jia Fei

Keywords:
Drilling and completion integration
Unified modeling
Multi-mechanism coupling
structural-state integrated damage function (SSIDF)
Feedback network
Structural disturbance function

ABSTRACT

To address the modeling fragmentation and predictive deviation caused by the conventional “single-mechanism, weakly coupled, additive response” approach in formation damage research, this study proposes an integrated modeling framework for multi-mechanism coupling throughout the entire drilling and completion process. Five dominant damage mechanisms are unified into a multi-physics formulation featuring a dual solid–liquid module architecture and a shared-state coupling mechanism. A structural-state integrated damage function (SSIDF) is introduced to establish a continuous mapping from microscopic mechanism evolution to macroscopic permeability degradation. A feedback network encompassing scaling, clay swelling, and water blocking is further developed, achieving bidirectional dynamic coupling among reaction kinetics, interfacial transport, and saturation fields, and representing one of the most systematic coupling schemes currently known. The model is solved via a space-time multi-scale optimization strategy, ensuring strong numerical stability and scalability. Field validation demonstrates a prediction accuracy of 98.6%, representing an improvement of over 8% compared to traditional additive models. The model is particularly applicable to unconventional reservoirs such as deepwater formations, where multi-mechanism damage evolves rapidly and conventional additive models fail to capture dynamic coupling behavior.

1. Introduction

“Energy independence” is both a guarantee of national strength and a cornerstone of security (Zou et al., 2020). Since the United States first proposed the concept of “energy independence” in 1973 (Abelson, 1973), it has focused on unconventional resources such as shale oil and gas, supported by complementary strategies, fiscal and legal frameworks. As a result, by 2018 the country achieved a net natural gas export volume of 1085 × 10^8 m^3. In contrast, China’s resource endowment and national conditions make it unsuitable to simply replicate the U.S. energy development model. Instead, China must rely on scientific planning and technological innovation to ensure that over 90% of domestic energy consumption is met by domestic production, thereby achieving the strategic goal of “energy independence”.

The development of electronic computer technology represents one of the hallmarks of the Third Technological Revolution. Within the upstream sector of the petroleum industry, the informatization and digitalization of oil and gas exploration and development directly determine drilling and completion efficiency, drilling encounter rates, and recovery factors. Numerical simulation research tailored to different blocks and development stages has gained broad international recognition and has become both a research hotspot and a frontier direction (Wang et al., 2023; Zhou et al., 2023). Drilling and completion are sequential yet interrelated steps in the exploitation of hydrocarbon reservoirs. Geological-engineering integration is thus an inevitable pathway for the efficient development of complex reservoirs, and

---

* Corresponding author.
E-mail address: m15600263100_1@163.com (G.-C. Jiang).
Peer review under the responsibility of China University of Petroleum (Beijing).

https://doi.org/10.1016/j.petsci.2026.01.007

integrated numerical simulation technology provides essential technical support.

As China extends its exploration and development activities into geologically complex reservoirs (Wen et al., 2023), multiple internal and external factors across drilling, completion, workover, fracturing, production, water injection, and polymer flooding stages disturb the original physical and chemical equilibrium of reservoirs. This leads to permeability reduction in both near-wellbore and far-field regions, blocking fluid flow and ultimately causing reservoir damage. Such damage, driven by different factors, results in significant economic losses and hydrocarbon losses, posing constraints on efficient reservoir exploration and development. Accurate diagnosis of the proportion of different types of reservoir damage, their spatial distribution, and temporal evolution can precisely guide drilling and completion design and the optimization of production enhancement measures. This, in turn, enhances the effectiveness of reservoir damage prevention and control, and in some cases, allows damage to be fully avoided. At present, reservoir damage diagnosis methods mainly include field-based diagnosis, core flooding experiments, numerical simulation (Bui et al., 2023; Cao et al., 2019; Cho et al., 2021; Ding, 2011), and machine learning approaches (Sheng and Jiang, 2023). Among these, numerical simulation can comprehensively account for reservoir damage mechanisms and influencing factors, dynamically simulate damage, and reduce the need for extensive physical-chemical experiments (Davarpanah et al., 2020). Compared with traditional field-based and core flooding methods, numerical simulation saves substantial time and costs (Jiang et al., 2022); compared with data-driven machine learning approaches, it eliminates dependence on historical data.

Over the past decade, numerous scholars have employed advanced experimental equipment and observation methods (Kargozarfard et al., 2023)—such as nuclear magnetic resonance (NMR) (Wu et al., 2019), tracer technology, X-ray scanning (Xiong et al., 2022), mass spectrometry (Rezaeizadeh et al., 2021), and neutron scattering—to investigate single-factor damage at the pore scale (also referred to as small, meso-, or micro-scale). These studies have provided relatively clear insights into the mechanisms and characteristics of single-factor reservoir damage. Concurrently, physical simulation experiments have examined the mechanisms of inorganic scaling, water blockage (Li et al., 2022), and clay swelling (Han et al., 2020; Ngata et al., 2023). However, the causes of reservoir damage are highly complex and diverse. During production, the reservoir rock's pore structure, wettability, hydrodynamic field, temperature-pressure field, and mineralogical composition continually evolve, leading to time-dependent variations in damage mechanisms. Damage often spans long cycles and wide ranges, exhibiting both complexity and superimposed effects. In general, although previous studies have summarized qualitative understandings of single-factor reservoir damage mechanisms from experimental simulations, there remains a lack of systematic research into coupled multi-factor mechanisms and corresponding quantitative mathematical models.

Different types of reservoir damage, as distinct physicochemical processes, may or may not be coupled depending on the similarity of their underlying mechanisms. For example, the spatiotemporal characteristics of solid invasion and fine particle migration are comparable (Cui et al., 2022; Li et al., 2023), while those of water blockage (Li et al., 2022), inorganic scaling, and clay swelling are also comparable (Ngata et al., 2023). Therefore, establishing quantitative models that couple reservoir conditions, invading fluid properties, and reservoir-fluid compatibility is of critical importance. Such models must accurately describe the quantitative relationships among fluid viscosity, pressure differentials, clay mineral content, rock plasticity coefficients, water saturation distribution, and permeability. Doing so is vital for elucidating the interactions among multiple damage mechanisms, identifying controlling factors, and clarifying the distribution and evolution patterns of reservoir damage. These insights bear directly on the assessment of China's hydrocarbon potential, recoverable reserves, production capacity, and the evaluation of reservoir "sweet spots".

Building on the multiple physicochemical processes that reservoirs undergo during drilling and completion, and drawing from the authors' prior systematic reviews and quantitative modeling of representative damage mechanisms (Jiang et al., 2024; Jin et al., 2021; Xu and Jiang, 2018; Yang et al., 2016; Elimelech et al., 1995; Khilar and Fogler, 1998; Oddo and Tomson, 1994; Civan, 2007; Xu, 2019), this study addresses the limitations of traditional models in representing multi-mechanism co-evolution. We construct a coupled reservoir damage model tailored for integrated drilling–completion conditions, comprehensively covering typical damage processes such as solid particle migration and deposition, solute reactions and adsorption in the liquid phase, and water–rock interfacial interactions. The model is grounded in mass conservation, Darcy flow, and multicomponent transport equations. It is modularized into solid-phase and liquid-phase mechanisms, with permeability, porosity, and water saturation serving as shared state variables to enable cross-mechanism field coupling. In the solid-phase module, solid invasion and particle migration are coupled through permeability perturbation to represent clogging and redistribution behaviors. In the liquid-phase module, a joint "scaling–swelling–water blockage" model is developed, in which ion concentration fields drive dynamic adjustment of membrane exchange coefficients, thereby capturing multiphysical feedback pathways.

On this basis, a unified structural-state integrated damage function (SSIDF) is further proposed. By treating pore structure evolution as a unifying mediator, the SSIDF maps multi-mechanism outputs into unified permeability evolution and macroscopic damage indices. This breaks the conventional paradigm of "mechanism separation and additive responses", and instead establishes an integrated pathway linking mechanism-driven processes, structural responses, and overall damage characterization. For numerical implementation, an explicit-weak iterative strategy optimized for modular coupling is adopted, effectively balancing physical completeness of mechanisms with computational complexity and convergence costs. Under multi-scale spatiotemporal conditions, the model demonstrates strong stability and scalability, offering a unified theoretical framework and modeling tool for quantitative prediction of reservoir damage, analysis of synergistic mechanisms, and identification of controlling responses (Fig. 1).

2. Mathematical model of single-factor reservoir damage

Each single-mechanism model developed in this section is based on several common physical assumptions to ensure tractability and numerical stability. The reservoir matrix is considered homogeneous and isotropic, with slightly compressible rock and fluid phases. Mechanical deformation and fracture propagation are neglected, as the study focuses on physicochemical formation damage rather than structural failure. These simplifications are consistent with near-wellbore conditions where permeability evolution is dominated by multiphase transport and reactive processes. Additional mechanism-specific assumptions are stated within each subsection where relevant.

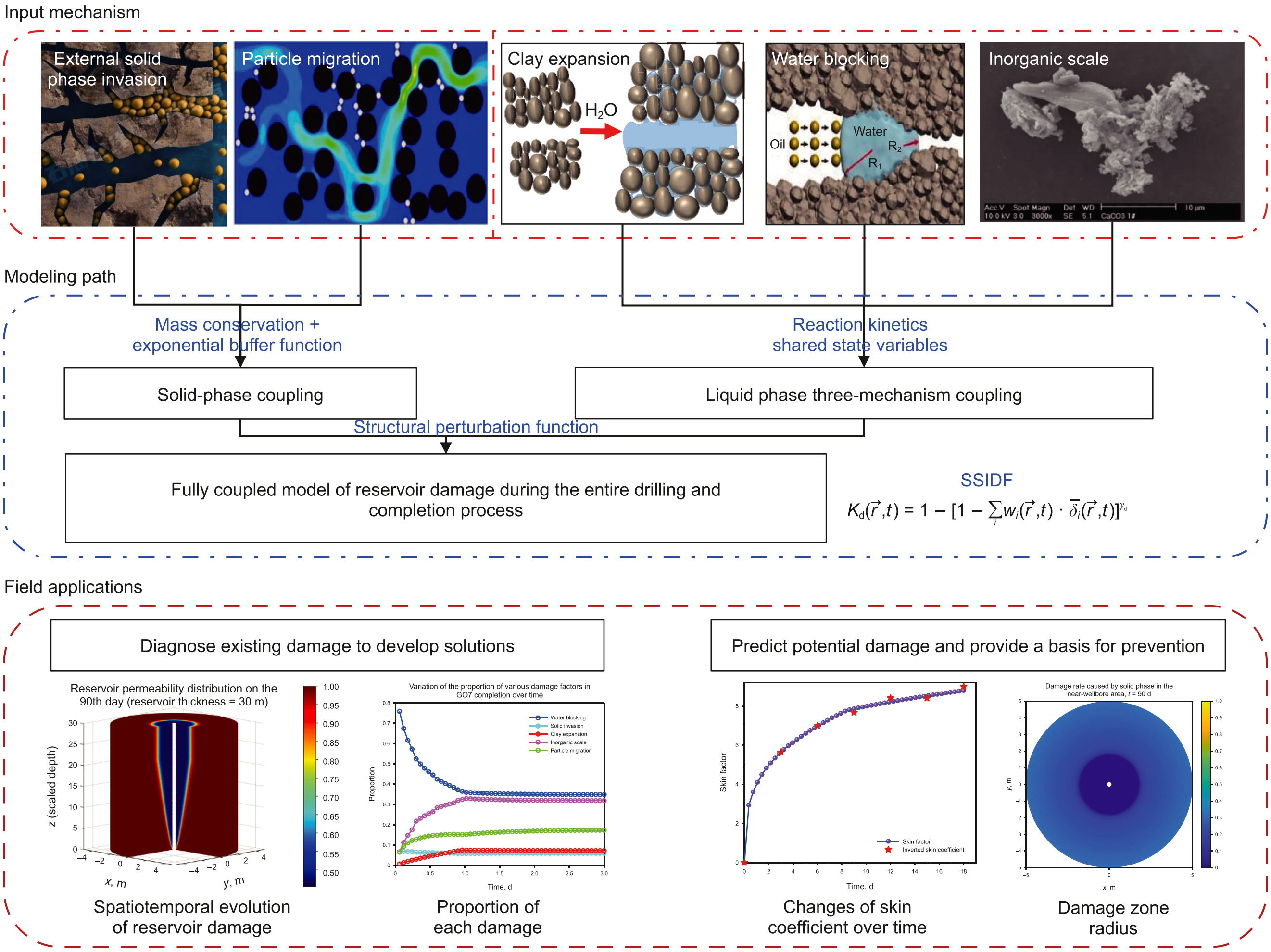

Fig. 1. Graphical abstract.

2.1. Governing equations of solid-phase damage

Solid-phase damage is governed by particle invasion and migration during drilling and completion. The process is described by a two-phase mass-balance model (Fig. 2) as formulated below.

The pressure gradient drives the solid–liquid flow and is described by Eqs. (1) and (2).

$$\nabla^2 P(\mathbf{r},t) = \frac{\varphi \mu c_t}{K(\mathbf{r},t)} \frac{\partial P(\mathbf{r},t)}{\partial t} \tag{1}$$

$$v(\mathbf{r},t) = -\frac{\tau K(\mathbf{r},t)}{\mu \varphi} \nabla P(\mathbf{r},t) \tag{2}$$

The mass-balance relations for mobile and deposited particles are summarized in Eqs. (3–6).

$$\frac{\partial}{\partial t}(\rho \varphi w(\mathbf{r},t)) + \nabla(\rho u(\mathbf{r},t) \cdot w(\mathbf{r},t) + j(\mathbf{r},t)) = -\dot{m} \tag{3}$$

$$j(\mathbf{r},t) = -\varphi \rho_L D \nabla w(\mathbf{r},t) \tag{4}$$

$$D(\mathbf{r},t) = \alpha v(\mathbf{r},t) \tag{5}$$

$$\dot{m} = \frac{\partial m(\mathbf{r},t)}{\partial t} = k(\mathbf{r},t)(\rho u(\mathbf{r},t) \cdot w(\mathbf{r},t) + j(\mathbf{r},t)) \tag{6}$$

In Eq. (6), k is the filtration coefficient, which has a relationship with temperature as expressed in Eq. (7). Elevated temperatures intensify the motion of solid particles, making them less likely to deposit or adsorb onto the internal surfaces of porous media. Therefore, k is negatively correlated with temperature.

$$k(\mathbf{r},t) = k_0 \left(1 - \frac{C_d(\mathbf{r},t)}{C_{dmax}}\right)^{m_k} e^{A_k\left(\frac{1}{T-T_{ik}} - \frac{1}{T-T_{ck}}\right)} \tag{7}$$

Eq. (7) models the filtration coefficient $k(\mathbf{r},t)$ as the product of a baseline term and two physically motivated modifiers. k_0 is the reference filtration coefficient under low-temperature, low-deposition conditions. The factor $\left(1 - \frac{C_d}{C_{dmax}}\right)^{m_k}$ introduces a saturation/self-limiting effect: as the local deposited-particle volume fraction C_d approaches the maximum packing C_{dmax}, the effective filtration pathway is reduced and k decreases; the exponent m_k controls the curvature of this decline based on pore-scale topology. The exponential term captures the temperature modulation of particle adhesion/retention through a shifted Arrhenius-type dependence, where A_k is a temperature-sensitivity factor and (T_{ik}, T_{ck}) are near-wellbore and reservoir reference temperatures, respectively. For $A_k > 0$, higher local temperatures (relative to the references) weaken solid–solid/solid–fluid adhesion and hence reduce k, consistent with core-flood observations.

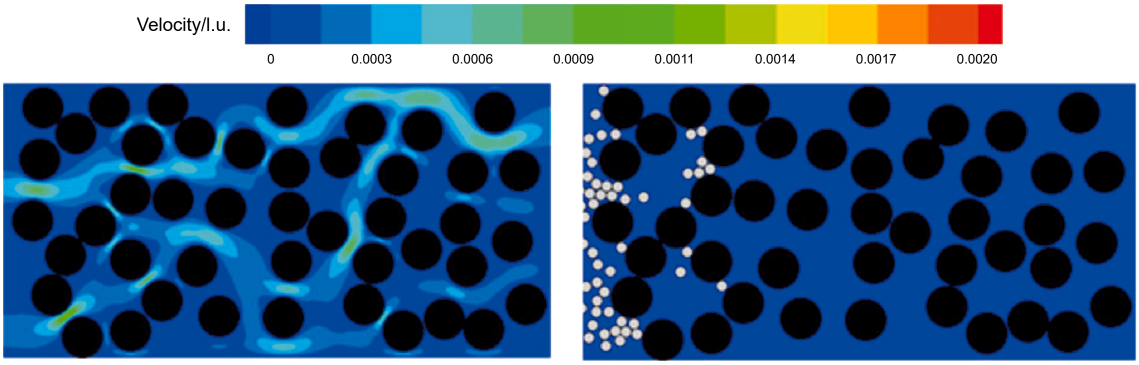

Porosity of porous media 0.6

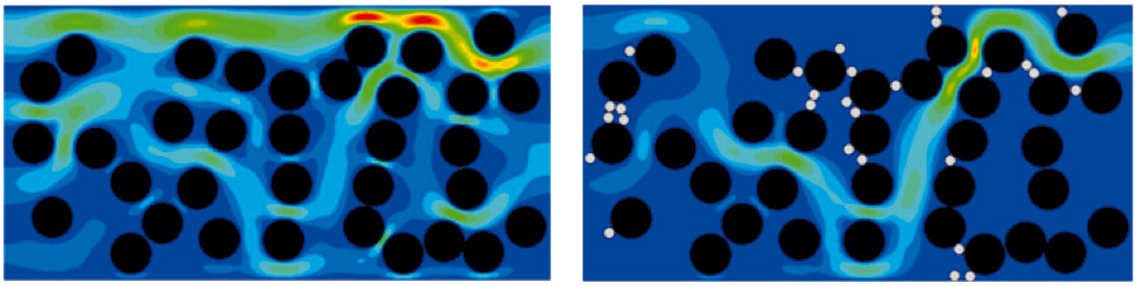

Porosity of porous media 0.7

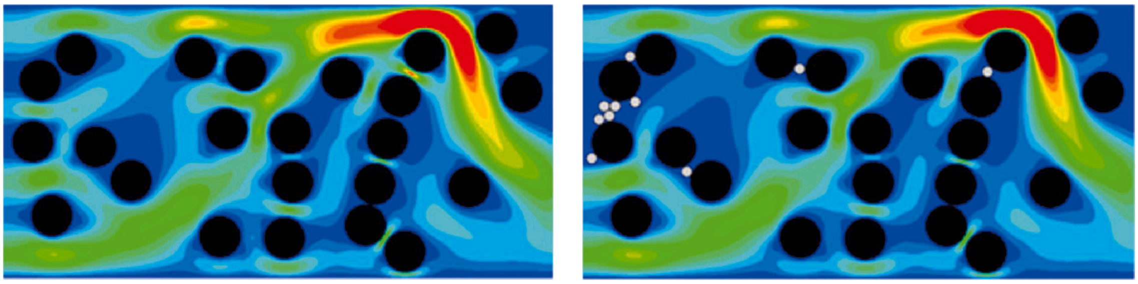

Porosity of porous media 0.8

Fig. 2. Effect of particle migration and deposition on fluid flow under different porosities (Jin et al., 2021).

From the structure of the deposition Eqs. (6) and (7), it can be seen that the magnitude of k_0 has a significant effect on the deposition rate (Xu and Jiang, 2018). The value of k_0 is determined by a set of dimensionless numbers, whereby the abundant physicochemical interactions between particles and the porous medium are introduced into the model through k_0 (Xu, 2019), as expressed in Eq. (8). In Eq. (8), η_s denotes the ideal particle capture efficiency under the dominance of physical forces, without considering adhesion effects. Therefore, Eq. (8) incorporates a correction factor to adjust for adhesion efficiency, taking into account both particle–particle (C–C) interactions and particle–medium interactions. In Eq. (8), θ represents the corrected porosity. Since porosity φ is a three-dimensional volumetric ratio, while many geometric parameters (such as specific surface area per unit volume) are related to particle linear scale, taking the cube root of $1-\varphi$ (the solid volume fraction) effectively converts a "volume ratio" into a "linear ratio", thereby enhancing the geometric rationality of the model. $N_{(\ldots)}$ represents a set of dimensionless numbers, with their expressions listed in Table 1.

Table 1
Dimensionless parameters including solid-phase deposition driving factors and their expressions.

Parameter name	Expression
N_R (radius number)	D_p/D_g
N_{Pe} (peclet number)	uD_g/D_∞
N_A (attraction number)	$H/(12\pi\mu\ R_p^2\ u)$
N_{DL} (double-layer number)	$\kappa_E R_p$
N_{E1} (first electrostatic force number)	$\upsilon_0 R_p(\zeta_p^2+\zeta_g^2)/(4k_B T)$
N_{E2} (second electrostatic force number)	$2(\zeta_p/\zeta_g)[1+(\zeta_p/\zeta_g)^2]$
N_G (gravity number)	$2\ R_p^2\ (\rho_P-\rho_L)g/(9\mu u)$
N_{Lo} (London force number)	$H/(6k_B T)$
N_{van} (Van der Waals number)	$H/(k_B T)$

$$k_0=\frac{3}{2}\frac{(1-\varphi)}{D_g}\beta_1\eta \tag{8}$$

$$\eta=\eta_s e^{\frac{\ln\alpha_{C-C}+\ln\alpha_{B-T}}{2}}$$

Table 2
Liquid-phase damage mechanisms.

Damage type	Characteristic $R_i(C)$	Main damage mechanism
Inorganic scaling	Reaction-kinetics type: $k_i\,C_i^{\beta_i}C_j^{\beta_j}$	Formation of solid-phase deposits blocking pore channels
Clay swelling	Ion diffusion and exchange	Pore-throat closure
Water blocking effect	Includes water saturation gradient term	Reduction of relative permeability

$$\eta_\mathrm{s}=2.4A_\mathrm{s}^{1/3}N_\mathrm{R}^{-0.081}N_\mathrm{Pe}^{-0.715}N_\mathrm{van}^{0.052}+0.55A_\mathrm{s}N_\mathrm{R}^{1.675}N_\mathrm{A}^{0.125}+0.22N_\mathrm{R}^{-0.24}N_\mathrm{G}^{1.11}N_\mathrm{van}^{0.053}$$

$$\alpha_\mathrm{C-C}=0.024N_\mathrm{DL}^{0.969}N_\mathrm{E1}^{-0.423}N_\mathrm{E2}^{2.88}N_\mathrm{Lo}^{1.5}+3.176A_\mathrm{s}^{1/3}N_\mathrm{R}^{-0.081}N_\mathrm{Pe}^{-0.715}N_\mathrm{Lo}^{2.678}+0.222A_\mathrm{s}N_\mathrm{R}^{3.041}N_\mathrm{Pe}^{-0.514}N_\mathrm{Lo}^{0.125}+N_\mathrm{R}^{-0.24}N_\mathrm{G}^{1.11}N_\mathrm{Lo}$$

$$A_\mathrm{s}=2\left(1-\theta^5\right)\Big/\left(2-3\theta+3\theta^5-2\theta^6\right),\theta=(1-\varphi)^{\frac{1}{3}}$$

$$\alpha_\mathrm{B-T}=0.002527N_\mathrm{DL}^{1.352}N_\mathrm{E1}^{-0.3121}N_\mathrm{E2}^{3.5111}N_\mathrm{Lo}^{0.7031}$$

The permeability damage rate and skin factor are defined by Eqs. (9) and (10).

$$K_\mathrm{d}(\boldsymbol{r},t)=\frac{K_0(\boldsymbol{r})}{K(\boldsymbol{r},t)}=\left(1-\frac{C_\mathrm{d}(\boldsymbol{r},t)}{C_\mathrm{dmax}}\right)^{m_K}\mathrm{e}^{A_k\left(\frac{1}{T-T_{ik}}-\frac{1}{T-T_{ck}}\right)} \tag{9}$$

$$S(\boldsymbol{r},t)=\left(\overline{K_\mathrm{d}(\boldsymbol{r},t)}^{-1}-1\right)\ln\left(\frac{r_\mathrm{s}}{r_\mathrm{w}}\right) \tag{10}$$

2.2. Mechanism-oriented modeling of solid-phase damage and specification of initial and boundary conditions

2.2.1. Exogenous solid particle invasion

Considering the case where the volume concentration of deposited particles $C_\mathrm{d}\approx0$, and the instantaneous porosity $\varphi=\varphi_0-C_\mathrm{d}$, $\partial\varphi=0$, by substituting the relationship between the volume concentration of mobile particles and their mass fraction ($w(\boldsymbol{r},t)=\frac{\rho_\mathrm{P}}{\rho_\mathrm{L}}C(\boldsymbol{r},t)$), and the relationship between Darcy apparent velocity and mixture phase velocity ($u(\boldsymbol{r},t)=\frac{\varphi v(\boldsymbol{r},t)}{\tau}$), into Eqs. (3) and (6), one can obtain the governing equation set for mobile particle concentration (Eq. (11)) and the governing equation set for deposited particle concentration (Eq. (12)). Eqs. (1, 2, 9–12) together constitute the governing system for exogenous solid particle invasion damage. The corresponding initial and boundary conditions can be expressed as in Eq. (13).

$$\begin{gathered}\frac{\partial C(\boldsymbol{r},t)}{\partial t}-\alpha v(\boldsymbol{r},t)\nabla^2C(\boldsymbol{r},t)+\frac{v(\boldsymbol{r},t)}{\tau}\left\{1-\left[1-\frac{\rho_\mathrm{P}}{\rho_\mathrm{L}}C(\boldsymbol{r},t)\right]k\alpha\tau\right\}\\ \nabla C(\boldsymbol{r},t)=\left(\frac{\rho_\mathrm{P}}{\rho_\mathrm{L}}C(\boldsymbol{r},t)-1\right)C(\boldsymbol{r},t)\end{gathered} \tag{11}$$

$$\frac{\partial C_\mathrm{d}(\boldsymbol{r},t)}{\partial t}=\frac{vk\phi}{\tau}\left[C(\boldsymbol{r},t)-\alpha\tau\nabla C(\boldsymbol{r},t)\right] \tag{12}$$

Eqs. (1, 2, 9–12) constitute the governing equations for controlling formation damage caused by the intrusion of external solid phases, while the initial and boundary conditions can be expressed in Eq. (13).

$$\begin{cases}C(\boldsymbol{r},t=0)=C_\mathrm{d}(\boldsymbol{r},t=0)=0\\ \Gamma_\mathrm{in}:=\left\{\boldsymbol{r}\in\mathbb{R}^3\,\middle|\,\|\boldsymbol{r}\|=r_\mathrm{w}\right\}\\ \Gamma_\mathrm{out}:=\left\{\boldsymbol{r}\in\mathbb{R}^3\,\middle|\,\|\boldsymbol{r}\|=r_\mathrm{s}\right\}\\ C(\boldsymbol{r},t)=\beta^*C_0(\boldsymbol{r},t), & \boldsymbol{r}\in\Gamma_\mathrm{in},t>0\\ C(\boldsymbol{r},t)=0, & \boldsymbol{r}\in\Gamma_\mathrm{out},t>0\\ P(\boldsymbol{r},t)=P_\mathrm{in}, & \boldsymbol{r}\in\Gamma_\mathrm{in},t>0\\ P(\boldsymbol{r},t)=P_\mathrm{out}, & \boldsymbol{r}\in\Gamma_\mathrm{out},t>0\end{cases} \tag{13}$$

It should be emphasized that the inner boundary condition of C is not directly defined by the solid-phase concentration C_0 of the invading fluid. Instead, the concept of particle "transmission probability" is introduced, accounting for the constraint imposed by the matching between particle size and pore throat size. Since the solid phase in drilling fluids exhibits a particle size distribution, and reservoir pores also possess a mean pore radius and distribution characteristics (Eq. (14)), the mean pore radius can be expressed as $\boldsymbol{r}=\mathrm{e}^{\mu_\mathrm{s}+\frac{\sigma_\mathrm{s}^2}{2}}$, with a standard deviation of $\mathrm{SD}=\boldsymbol{r}\sqrt{\mathrm{e}^{\sigma_\mathrm{s}^2}-1}$. Only particles with radii smaller than the corresponding pore radius can penetrate into the reservoir. Therefore, only a fraction $\beta(r_\mathrm{o})$ of particles in C_0 can enter the formation, where these particles have radii smaller than r_o. The parameter β can be calculated by Eq. (15).

$$N(r;\mu_\mathrm{s},\sigma_\mathrm{s})=\frac{1}{\sigma_\mathrm{s}\sqrt{2\pi}}\mathrm{e}^{-\frac{(\ln r-\mu_\mathrm{s})^2}{2\sigma_\mathrm{s}^2}} \tag{14}$$

$$\mu_\mathrm{s}=\ln\left[\frac{\bar{r}}{\sqrt{1+\left(\frac{\mathrm{SD}}{\bar{r}}\right)^2}}\right]$$

$$\sigma_\mathrm{s}=\sqrt{\ln\left[1+\left(\frac{\mathrm{SD}}{\bar{r}}\right)^2\right]}$$

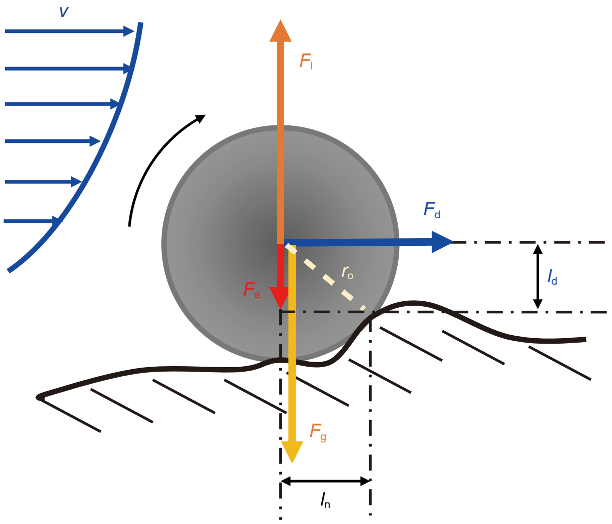

Fig. 3. Force diagram of particle mobilization on the pore surface in porous media.

$$\beta(r_o) = 1 - \frac{1}{\sqrt{\pi}} \int_{-\frac{\ln r_o - \mu_s}{\sigma_s \sqrt{2}}}^{\infty} e^{-x^2} dx \tag{15}$$

For instance, when a formation has $\bar{r} = 6$ μm and SD = 6 μm, the transmission probability for particles with a radius of 4 μm is 5.08%. If SD decreases to 3 μm, the probability rises to 46.15%. This result reflects the degree of dispersion in pore radii relative to the mean pore size. A smaller SD indicates that pore sizes are more narrowly distributed around the mean, implying a more homogeneous reservoir structure. Under such conditions, most pore radii exceed the mean radius, facilitating the entry of small particles. Conversely, a larger SD corresponds to a broader pore size distribution, lowering the transmission probability for particles smaller than the mean pore radius. For larger particles, the trend is reversed: in formations with a small SD, their entry probability is low, while a larger SD allows more large pores, increasing the likelihood of particle penetration. Thus, pore size distribution heterogeneity exerts opposite effects on the transmission behavior of small and large particles. Furthermore, the solid-phase particles within the wellbore themselves follow a particle size distribution. Therefore, when calculating the transmission probability, both pore throat radii and particle size distributions must be considered simultaneously. If the solid-phase distribution of the invading fluid is defined as $N_s(r_{so};\ \mu_{so},\ \sigma_{so})$, the new interception probability is given by Eq. (16), which is then substituted into the boundary condition to form Eq. (13).

$$\beta^* = 1 - \frac{1}{\sqrt{\pi}} \int_0^{\infty} N(r_{so}; \mu_{so}, \sigma_{so}) \int_{-\frac{\ln r_o - \mu_s}{\sigma_s \sqrt{2}}}^{\infty} e^{-x^2} dx dr_{so} \tag{16}$$

2.2.2. Particle migration

The structural framework of the particle migration model is similar to that of solid-phase invasion, except that the particle sources originate from within the reservoir and their generation depends on flow intensity and the critical velocity. As illustrated in Fig. 3, under the combined effects of fluid scouring and interactions with the rock surface, particles are subjected to drag force (F_d), gravity (F_g), electrostatic force (F_e), and lift force (F_l). The critical velocity corresponds to the fluid velocity at which these forces and torques reach equilibrium.

Based on torque balance (Xu and Jiang, 2018) and DLVO theory (Yang et al., 2016; Elimelech et al., 1995; Khilar and Fogler, 1998), the implicit equation for the critical velocity v_c can be derived (Eq. (17)). As indicated by Eq. (17), the magnitude of the critical velocity is jointly influenced by the mechanical, physical, and chemical properties of both the particles and the porous medium. When the critical velocity is known, primary particles can be mobilized only if the local fluid velocity in the reservoir exceeds this threshold, thereby becoming a source of migrating material. Considering that fluid velocity is relatively high near the wellbore, the particle mobilization region is mainly distributed within an annular zone surrounding the borehole.

$$v_c = \frac{r_c}{3\omega\pi\mu r_s^2} \cdot \frac{\frac{4}{3}\pi(\rho_s - \rho_L) r_s^3 - \chi \sqrt{27\rho\mu \left(\frac{r_s^2 v_c}{r_c}\right)}^3 - \nabla V(h)}{\left[\left(\frac{4Kr_s^2}{\frac{4}{3}\pi(\rho_s - \rho_L) r_s^3 - \chi \sqrt{27\rho\mu \left(\frac{r_s^2 v_c}{r_c}\right)}^3 - \nabla V(h)}\right)^{\frac{2}{3}} - 1\right]^{\frac{1}{2}}} \tag{17}$$

Next, the release rate of particles from the pore matrix, denoted as q_s is considered. The functional form of q_s varies with reservoir conditions and drilling/completion processes, and its exact form is almost impossible to determine. Nevertheless, q_s is inherently a function of both time and space. Drawing on two physical intuitions—namely, "particle mobilization occurs within the annular region near the wellbore" and "the release duration of particles must be finite"—a spatiotemporal distribution function can be constructed, as shown in Eq. (18). As illustrated in Fig. 4, Eq. (18) characterizes a typical kinetic behavior that is "concentrated at early times, spatially enhanced near the wellbore, and exponentially decaying with time."

$$q_s(r,t) = \begin{cases} R_0 \cdot e^{-\beta_2 (r - r_w)} \cdot e^{-\alpha_1 t}, & v \geq v_c \\ 0, & v < v_c \end{cases} \tag{18}$$

Eq. (18) further indicates that when the fluid velocity exceeds the critical velocity, particles are mobilized and transported with the flowing fluid. The mobilized particles increase the mass of the fluid–solid mixture; however, since the deposition equation is independent of the particle source location, it remains unchanged. By introducing q_s into the right-hand side of Eq. (3), the governing equation for the concentration of migrating particles in the case of migration-induced damage (Eq. (19)) can be obtained. Together with Eqs. (1, 2, 9, 10, 12, 18 and 19), this forms the system of control equations for particle migration damage. At both the wellbore and reservoir boundaries, C=0, while the remaining initial and boundary conditions remain unchanged.

$$\frac{\partial C(\boldsymbol{r},t)}{\partial t} - \alpha v(\boldsymbol{r},t) \nabla^2 C(\boldsymbol{r},t) + \frac{v(\boldsymbol{r},t)}{\tau} \left\{ 1 - \left[1 - \frac{\rho_P}{\rho_L} C(\boldsymbol{r},t) \right] k\alpha\tau \right\} \nabla C(\boldsymbol{r},t) = \left[\frac{\rho_P}{\rho_L} C(\boldsymbol{r},t) - 1 \right] \left[\frac{k(\boldsymbol{r},t) v(\boldsymbol{r},t)}{\tau} C(\boldsymbol{r},t) - \frac{q_s(\boldsymbol{r},t)}{\rho_P \varphi} \right] \tag{19}$$

2.3. Unified modeling framework for liquid-phase damage

Liquid-phase damage is widely encountered during drilling and completion operations, primarily involving three mechanisms:

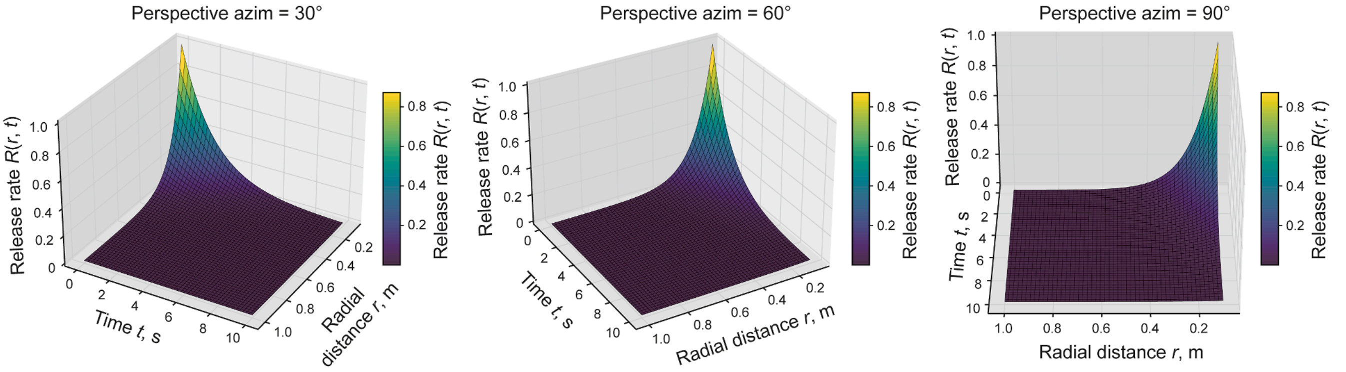

Fig. 4. Spatiotemporal distribution of particle release rate.

water-blocking effect, clay mineral swelling, and inorganic scale precipitation. Although their causes differ, they can all essentially be attributed to the diffusion and reaction of invading liquid phases within the formation, which subsequently alters pore structure and reduces permeability. Therefore, differentiated modeling approaches can be established under a unified framework of mass conservation and flow dynamics, enhancing descriptive consistency and facilitating subsequent coupled simulations.

To characterize the transport and reaction of liquid phases in porous media, the following system of governing equations is adopted: (1) Solute/solution transport equation (e.g., Eq. (20)); (2) Flow dynamics equation (Eqs. (1) and (21)); (3) Pore structure evolution equation (see Section 2.4).

$$\varphi\frac{\partial C_i}{\partial t} - \nabla\cdot(D\nabla C_i) + \nabla\cdot(uC_i) = -R_i(C) \tag{20}$$

$$u(\mathbf{r},t) = -\frac{K(\mathbf{r},t)}{\mu}\nabla P(\mathbf{r},t) \tag{21}$$

Under this unified system of governing equations, the key distinctions among different liquid-phase damage mechanisms primarily manifest in the source/sink term $R_i(C)$ and the mode of pore blockage (see Table 2).

2.4. Mechanism-oriented modeling of liquid-phase damage

2.4.1. Inorganic scale

In global oilfields, the most common types of inorganic scale primarily include calcium, strontium, and barium sulfate precipitates, as well as calcium carbonate scale. Reservoir damage caused by inorganic scaling is mainly associated with three key issues: (1) whether precipitation reactions occur; (2) the extent and rate of such reactions; and (3) the spatial distribution characteristics of precipitates within the reservoir. Current studies have largely concentrated on the thermodynamic conditions under which these reactions occur, whereas investigations into their kinetic processes and spatial evolution remain relatively limited. To address these issues, this study establishes a set of coupled mechanical–chemical differential equations aimed at revealing the spatiotemporal evolution of scale-induced damage.

Under specific temperature, pressure, and ionic concentration conditions, the occurrence of a given precipitation reaction in reservoir fluids can generally be determined using the saturation index (I_s). According to the Tomson-Oddo criterion (Oddo and Tomson, 1994), I_s can be expressed as Eq. (22).

$$I_s(P,T,S_{\text{ion}}) = \lg\left[\frac{[Cat][An]}{K_c(P,T,S_{\text{ion}})}\right] \tag{22}$$

When the saturation index $I_s \le 0$ at a given moment, the system is either undersaturated or saturated, and precipitation reactions cannot occur. In this case, the governing equation (Eq. (20)) excludes the precipitation term and describes only the physical transport of solutes. Precipitation reactions are thermodynamically feasible only when $I_s > 0$, indicating that the system has reached a supersaturated state. At this point, Eq. (20) must incorporate a reaction source term to simulate precipitation behavior. Therefore, at each time step, the model must dynamically evaluate the local saturation index to determine whether the precipitation term should be activated, as expressed in Eq. (23).

$$k_i = \begin{cases} 0, I_S \le 0 \\ k_{i0}, I_S > 0 \end{cases} \tag{23}$$

The parameter k_{i0} denotes the reaction rate constant for the i-th ionic precipitation reaction, and its value can be referenced from mineral salt-forming reactions. If the reaction occurs, the cumulative amount of precipitation within a time step $\mathrm{d}t$ is expressed in Eq. (24).

$$\mathrm{d}(\mathbf{r},t+\mathrm{d}t) = \mathrm{d}(\mathbf{r},t) + \frac{1}{\varphi}\sum_i \omega_i \Delta C_i(\mathbf{r},t) \tag{24}$$

$\Delta C(\mathbf{r},t)$ represents the variation in the concentration of the i-th ion within $\mathrm{d}t$ due to the reaction. The relationship can be expressed as: $\omega_i\Delta C(\mathbf{r},t) = k_i C_i^{\beta_i} C_j^{\beta_j}\mathrm{d}t$. Accordingly, Eq. (20) is specialized into Eq. (25). When calculating permeability damage, the cumulative concentrations of various precipitates must be multiplied by their respective molar masses and divided by their corresponding densities, thereby converting them into C_d. This value is then applied to Eq. (9) to compute permeability. Collectively, Eqs. (9, 21–25) constitute the spatiotemporal evolution model for inorganic scale damage. The initial condition is defined as the ionic concentration C_i within the reservoir, while the boundary condition is defined as the ionic concentration C_i in the invading fluid.

$$\varphi\frac{\partial C_i}{\partial t} = \nabla\cdot(D\nabla C_i) - \nabla\cdot(uC_i) - k_i C_i^{\beta_i} C_j^{\beta_j} \tag{25}$$

2.4.2. Clay swelling

The clay swelling damage process can be divided into two stages: The first stage involves the diffusion of the aqueous phase into the solid matrix after it contacts the pore rock surfaces,

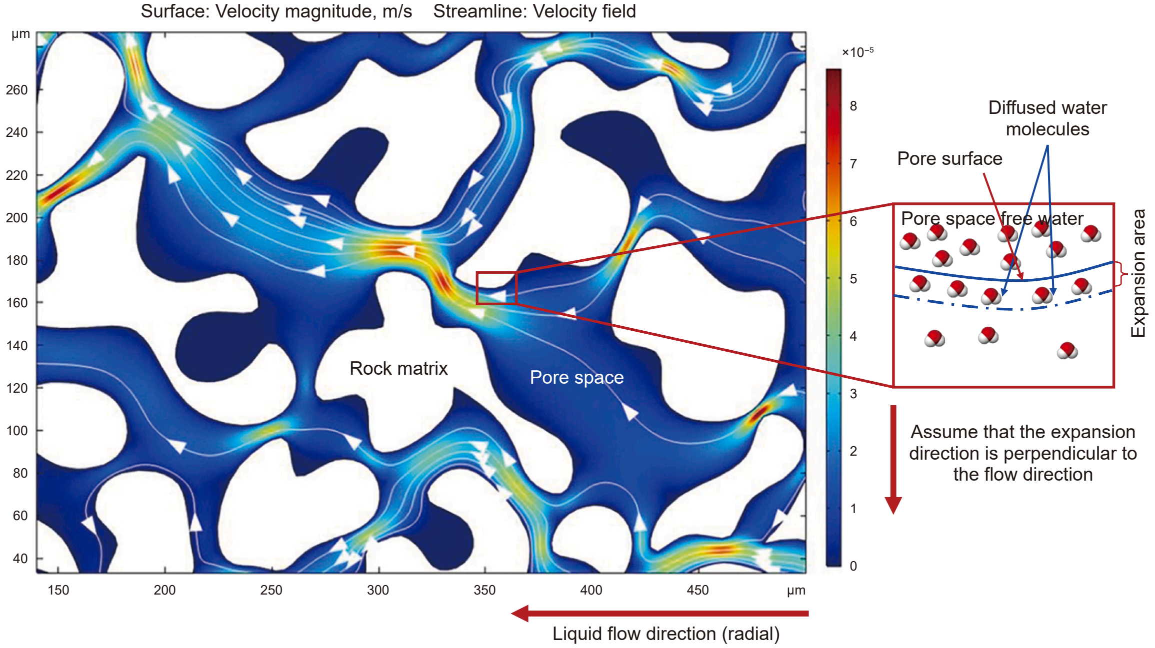

Fig. 5. Illustration of water-phase seepage and water molecule permeation at the solid–liquid interface in porous media.

penetrating into the interlayer of the clay structure and inducing volumetric expansion (as shown in Fig. 5). In the second stage, as the driving force for fluid flow weakens and the interfacial adsorption approaches saturation, the system gradually reaches a quasi-steady state, and the swelling rate significantly decreases. The first stage can be characterized using a diffusion model driven by the concentration gradient, while the second stage can be indirectly represented by the asymptotic behavior of the model solution over time.

According to Fick's law of diffusion, an equation can be established for the diffusion of water molecules into the pore matrix (Eq. (26)). For this type of diffusion-interface reaction problem, existing studies often employ Laplace transform methods to solve the equation. While this approach yields a formal analytical expression, its inverse transform typically involves non-elementary functions, making it difficult to obtain a clear, explicit solution. In this study, based on the classical diffusion solution provided by Civan (2007), a similarity variable transformation method is used to derive the diffusion-boundary reaction problem (see Appendix A). This derivation systematically reconstructs the solution formation process and clarifies the influence of boundary control terms on the analytical structure. This derivation not only validates the reasonableness of the solution but also provides a foundation for subsequent parameter analysis and model verification.

$$\frac{\partial c}{\partial t}=D\frac{\partial^2 c}{\partial z^2}, 0\le z<\infty, t\ge 0 \tag{26}$$

$$c(t=0)=c_0$$

$$\dot{S}\equiv -D\frac{\partial c}{\partial z}=\psi(c_1-c)|_{z=0}, \lim_{z\to\infty}c(z,t)=c_0$$

Under actual reservoir conditions, the water content in the pores is always greater than or equal to the water content in the solid matrix of the rock. Using the analytical solution (Eq. (27)) of Eq. (26) and introducing boundary constraints to represent the porosity change rate caused by clay swelling, as shown in Eq. (28), the clay swelling damage is not caused by particle deposition, and thus the damage rate is calculated using Eq. (29). Eqs. (9, 20, 21, 28 and 29) form the system of governing equations for clay swelling damage. The initial conditions are given by $\varphi(\boldsymbol{r},t=0)=\varphi_0$ and $c_1(\boldsymbol{r}, t=0)=\varphi_0 S_{\mathrm{wc}}$, and the boundary condition is $c_1(\boldsymbol{r},t)=\varphi_0$, where $\boldsymbol{r}\in\Gamma_{\mathrm{in}}$ (the rock near the wellbore is fully saturated with water).

$$c(z,t)=c_0+\frac{2}{\sqrt{\pi}}(c_1-c_0)\cdot\int_{\frac{z}{2\sqrt{Dt}}+\frac{\psi\sqrt{t}}{\sqrt{D}}}^{\infty}\mathrm{e}^{-x^2}\mathrm{d}x \tag{27}$$

$$-\frac{\partial\varphi}{\partial t}=\lambda\dot{S} \tag{28}$$

$$\dot{S}=\begin{cases}\frac{2}{\sqrt{\pi}}(c_1-c_0)\psi\mathrm{e}^{\frac{\psi^2}{D}t}\int_{\sqrt{\frac{\psi^2 t}{D}}}^{\infty}\mathrm{e}^{-x^2}\mathrm{d}x, & c_1>c_0\\ 0, & c_1\le c_0\end{cases}$$

$$K_{\mathrm{d}}(\boldsymbol{r},t)=\left[\frac{\varphi(\boldsymbol{r},t)}{\varphi_0}\right]^{m_K} \tag{29}$$

2.4.3. *Water blocking*

Water blocking damage is closely related to the topological parameters of porous media. In this study, a fractal rock model and linear Hagen-Poiseuille viscous flow are used to establish the water blocking damage model. The fractal dimension is calculated using Eq. (30).

$$D_{\mathrm{frac}}=3-\frac{\ln(1-\varphi)}{\ln(r_{\min})-\ln(r_{\max})} \tag{30}$$

The water phase saturation can be calculated using Eq. (31).

$$S_{\mathrm{w}}=\frac{c_1}{\varphi} \tag{31}$$

Based on the continuity of the pore throat distribution in a multipore medium, the linear Hagen-Poiseuille viscous flow is modified into an integral form (Eq. (32)). From this, the permeability damage rate can be calculated (Eq. (33)).

$$K(\boldsymbol{r},t)=\frac{\varphi(\boldsymbol{r},t)}{8\tau^2}\sum_i \xi_i r_i^2 \Rightarrow K(\boldsymbol{r},t)=\frac{\varphi(\boldsymbol{r},t)}{8\tau^2}\int r^2 \mathrm{d}\xi \tag{32}$$

$$\mathrm{d}\xi=\frac{\left(3-D_{\mathrm{frac}}\right)r^{2-D_{\mathrm{frac}}}}{r_{\max}^{3-D_{\mathrm{frac}}}\left[1-\left(\frac{r_{\min}}{r_{\max}}\right)^{3-D_{\mathrm{frac}}}\right]}\mathrm{d}r$$

$$K_{\mathrm{d}}(\boldsymbol{r},t)=\frac{1-\left(\frac{r_{\min}}{r_{\max}}\right)^{5-D_{\mathrm{frac}}}}{1-\left(\frac{r_{\min}}{r_{\max}}\right)^{3-D_{\mathrm{frac}}}}\cdot\frac{1-\left[1-\left(\frac{r_{\min}}{r_{\max}}\right)^{3-D_{\mathrm{frac}}}\right]S_{\mathrm{w}}-\left(\frac{r_{\min}}{r_{\max}}\right)^{3-D_{\mathrm{frac}}}}{1-\left\{\left[1-\left(\frac{r_{\min}}{r_{\max}}\right)^{3-D_{\mathrm{frac}}}\right]S_{\mathrm{w}}+\left(\frac{r_{\min}}{r_{\max}}\right)^{3-D_{\mathrm{frac}}}\right\}^{\frac{5-D_{\mathrm{frac}}}{3-D_{\mathrm{frac}}}}} \tag{33}$$

Eqs. (9) 20, 21,and 33) constitute the spatiotemporal evolution equation for water blocking damage. The initial condition for velocity is u=0, and the initial water phase saturation is $S_{\mathrm{w}}=S_{\mathrm{wc}}$. The pressure boundary condition is consistent with Eq. (13), with S_{w} ($\boldsymbol{r}$, t) = 1, for $\overrightarrow{r}\in\Gamma_{\mathrm{in}}$ (near the wellbore, where the rock is saturated with water).

3. Multimechanism coupled mathematical model of reservoir damage

Before constructing the coupled framework, it is necessary to clarify how the five single-mechanism models developed in Section 2 are integrated into a unified system. All individual mechanisms—solid invasion, particle migration, inorganic scaling, clay swelling, and water blocking—share a common mathematical foundation based on mass conservation, Darcy flow, and multicomponent transport equations.

The coupled SSIDF framework inherits the fundamental assumptions of the single-mechanism formulations, including isotropic matrix properties, slight compressibility of rock and fluids, and the exclusion of mechanical deformation. To achieve numerical stability, two additional simplifications are adopted: (1) weak coupling between the solid-phase mechanisms (solid invasion and particle migration), and (2) strong bidirectional coupling among liquid-phase mechanisms (scaling, swelling, and water blocking). These hierarchical simplifications balance physical realism with computational tractability and are suitable for typical near-wellbore conditions dominated by physicochemical interactions rather than large-scale mechanical failure.

Their coupling is achieved through a set of shared state variables, primarily permeability (K), porosity (φ), and water saturation (S_{w}), which serve as the bridges linking local physicochemical processes to global permeability evolution. On this basis, the integration proceeds hierarchically:

(1) the two solid-phase processes are first weakly coupled via permeability perturbation to represent mutual restriction during particle deposition and migration;
(2) the three liquid-phase processes are then strongly coupled through feedback loops that dynamically exchange hydrodynamic, chemical, and structural variables;
(3) finally, the SSIDF consolidates all mechanisms into a unified macroscopic representation.

This hierarchical integration ensures both physical consistency and computational tractability, forming the foundation of the coupled framework described below (Fig. 6).

3.1. Coupling method for solid-phase damage

To gain a deeper understanding of the interactions among multiple damage mechanisms in the near-wellbore region during drilling, a numerical coupling model between solid-phase invasion and particle migration is established in this study. This model preserves the original physical processes and numerical schemes of each mechanism, while introducing coupling control through a structured parameter-transfer approach, thereby enabling dynamic simulation of the interactions among damage processes.

A weak coupling strategy is adopted for the solid-phase coupling model. The solid-phase invasion module employs particle screening and adsorption–deposition theory to calculate the dimensionless permeability distribution at different time steps. To reduce computational complexity and avoid mismatches in spatiotemporal dimensions, an average influence factor is defined (Eq. (34)). This factor retains the spatial distribution characteristics but takes the arithmetic mean in the temporal dimension, and is then introduced as an input parameter for the particle migration module.

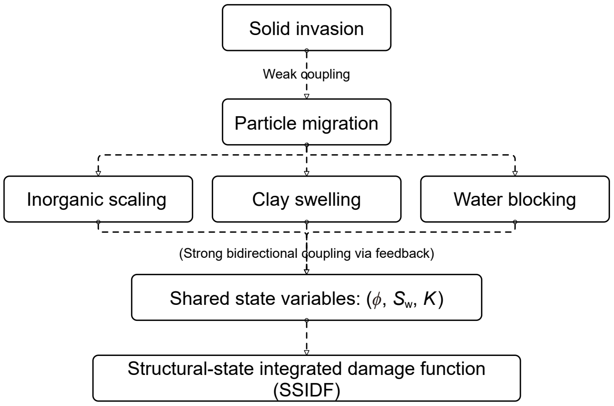

Fig. 6. Coupling relationships among five single-mechanism models in the SSIDF framework.

$$\overline{K}_{\mathrm{d}}^{\mathrm{G}}(\boldsymbol{r}) = \frac{1}{N_t}\sum_{i=1}^{N_i} K_{\mathrm{d}}^{\mathrm{G}}(\boldsymbol{r}, t_i) \tag{34}$$

The particle migration model is solved using an explicit difference scheme for the processes of particle advection, dispersion, and deposition. With the introduction of coupling, the boundary condition for particle injection concentration in the original model is governed by Eq. (35).

$$C(\boldsymbol{r}, t) = \beta^{*} C_0(\boldsymbol{r}, t)\cdot\phi\left(\overline{K}_{\mathrm{d}}^{\mathrm{G}}(\boldsymbol{r})\right), \boldsymbol{r}\in\Gamma_{\mathrm{in}}, t>0 \tag{35}$$

Here, $\phi(x)$ is a coupling function that characterizes the regulatory effect of external solid-phase blockage on particle migration. To ensure both physical rationality and numerical stability, an exponential buffering function is adopted, as given in Eq. (36).

$$\phi\left(\overline{K}_{\mathrm{d}}^{\mathrm{G}}(\boldsymbol{r})\right) = \mathrm{e}^{-\gamma\left(1-\overline{K}_{\mathrm{d}}^{\mathrm{G}}(\boldsymbol{r})\right)} \tag{36}$$

The coupling strength factor γ physically controls the degree of permeability suppression imposed by solid-phase deposition on subsequent particle migration. It reflects how rapidly the permeability perturbation propagates through the solid matrix during coupling iteration. In this study, γ is empirically set to 3, corresponding to a moderate coupling intensity where permeability reduction below 0.5 leads to a 60%–70% decrease in migration flux. Larger γ values (>5) represent stronger coupling typical of fine-grained formations with high solids retention, whereas smaller values (1–2) correspond to weak coupling observed in coarse sandstones.

The value of γ can be calibrated through two approaches: (1) laboratory core flooding tests by fitting the time-dependent permeability decline curves, or (2) history matching against field-measured skin factor evolution.

3.2. Establishing the asymmetric feedback mechanism of liquid-phase damage

It is important to clarify the rationale behind the different coupling strategies adopted for solid-phase and liquid-phase mechanisms. The two solid-phase processes—solid invasion and particle migration—operate on relatively distinct spatial and temporal scales: solid invasion mainly alters permeability through pore plugging near the wellbore, whereas particle migration occurs as a secondary redistribution over longer time scales. Because their mutual influence is indirect and largely mediated by the evolving permeability field, a weak (one-way) coupling is sufficient to capture the dominant feedback while maintaining numerical stability and tractability.

In contrast, the three liquid-phase mechanisms—scaling, swelling, and water blocking—share common state variables such as porosity (φ), water saturation (S_{w}), and ion concentration (C_{i}), and their interactions are highly nonlinear and simultaneous. Scaling alters ion concentrations and pore geometry, which directly affect water-blocking behavior; swelling modifies φ and in turn changes hydrodynamic and chemical responses. These processes therefore require a strong (two-way) coupling realized through the feedback network, ensuring accurate representation of cross-mechanism effects.

This hierarchical coupling strategy achieves a balance between physical realism and numerical robustness: weak coupling avoids excessive stiffness in the solid-phase module, while strong coupling among liquid-phase processes preserves the fidelity of rapid physicochemical interactions.

Under the combined influence of multiple factors, liquid-phase behavior in the near-wellbore region significantly affects the permeability evolution process. Water blocking, inorganic scale, and clay swelling damage are all driven by aqueous-phase dynamics. Together, they influence pore water content and the integrity of flow channels, making them physically highly coupled. This section provides a detailed discussion of the modeling methodology for such coupling mechanisms.

3.2.1. One-way coupling of “scaling–swelling”

According to the fundamental theory of fluid flow in porous media, particularly the Kozeny–Carman equation and the capillary bundle model, permeability is proportional to the fourth power of pore throat radius. Thus, within the range of positive real values, permeability is a strictly convex function of pore throat radius, and marginal effects increase with reduction in radius. For example, when the pore throat radius decreases from 3 to 2 μm, the permeability drops to 19.75% of its original value; whereas when the radius further decreases from 2 to 1 μm, the permeability decreases to only 6.25% of its original value, indicating a slowing decline. On the other hand, when inorganic scaling damage is severe, the initial ion concentration is relatively high, which significantly affects the membrane mass exchange coefficient ψ for water entry into clay minerals (Eq. (26)), thereby influencing clay swelling behavior. The relationship of ψ is given in Eq. (37).

$$\psi = \alpha_0 D^{\frac{2}{3}}\left(\frac{1}{\mu}\right)^{\frac{1}{3}}\left(\frac{1}{r_{\mathrm{m}}\kappa}\right)^{\frac{2}{3}}\left[1-\frac{2I_1(r_{\mathrm{m}}\kappa)}{r_{\mathrm{m}}\kappa I_0(r_{\mathrm{m}}\kappa)}\right]^{\frac{1}{3}} \tag{37}$$

$$I_0(x) = \sum\nolimits_{i=0}^{\infty}\frac{1}{(i!)^2}\left(\frac{x}{2}\right)^{2i}$$

$$I_1(x) = \sum\nolimits_{i=0}^{\infty}\frac{1}{i!(i+1)!}\left(\frac{x}{2}\right)^{2i+1}$$

$$\kappa = \sqrt{\frac{\mathrm{e}^2\sum\nu_i z_i^2}{\varepsilon_0 D_e k_B T}}$$

Using Eq. (37), the variation of the membrane mass exchange coefficient with inverse Debye length was calculated under a viscosity range of 10–60 mPa·s, as shown in Fig. 7, revealing a negative correlation. According to the definition of inverse Debye length κ in Eq. (37), the higher the electrolyte concentration (ionic content) in the solution, the larger κ, and hence the smaller the Debye length. In core samples, when clay minerals undergo clay swelling, increasing the salinity of drilling fluid filtrate effectively shortens the Debye length κ^{-1} on solid surfaces, thereby suppressing the diffusion rate of water molecules into clay structures and reducing

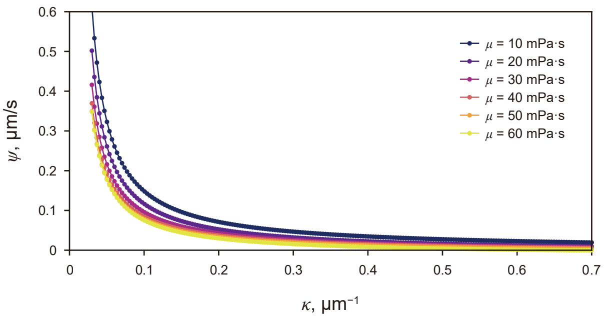

Fig. 7. Variation of membrane mass transfer coefficient with inverse Debye length of solid surfaces for invading fluids of different viscosities.

the swelling degree. This mechanism aligns well with experimental observations and field practices. In actual applications, high-concentration potassium chloride is often added to drilling fluids to effectively inhibit clay swelling.

In summary, based on the unified liquid-phase governing equation system (Eqs. (20) and (21)), this study proposes a mechanism-driven "scaling–swelling" deeply coupled modeling method. Both mechanisms represent pore structure evolution driven by ion migration—one through the formation of solid precipitates and the other through volumetric expansion caused by interfacial water molecule diffusion–exchange—thus jointly influencing permeability changes. The core idea is as follows: at each time step, the inorganic scaling model (Eq. (25)) is first solved to obtain the ion concentration field at each spatial location. Subsequently, the salinity is calculated and substituted into the formula for the membrane mass exchange coefficient (Eq. (37)), thereby updating the ψ value in the clay swelling model (Eq. (28)) and dynamically adjusting the diffusion rate. This physical feedback channel reveals the controlling effect of solution salinity on swelling rates, namely, higher ionic strength suppresses further water molecule diffusion into interlayer structures, thereby mitigating swelling.

This "one-way physical driving + intra-time-step feedback loop" mechanism more effectively captures the nonlinear response behavior of real reservoirs compared to conventional sequential module coupling methods. The proposed "scaling–swelling" model further shares porosity fields and water saturation variables with the water blocking model, thus forming a unified coupling framework for liquid-phase damage.

3.2.2. *Construction of a two-way feedback model for "scaling–swelling–water blocking"*

In the mechanisms of liquid-phase reservoir damage, water blocking, inorganic scale precipitation, and clay mineral swelling exhibit significant physicochemical coupling effects. Their interactions are not merely unidirectional dependencies but instead form a dynamic nonlinear system through the sharing of state variables and interactive feedback pathways. Building upon the previously developed weakly coupled "scaling–swelling" model, this study further establishes a strongly coupled three-mechanism framework with feedback effects, thereby enabling a unified description of local hydrodynamics, chemical reactions, and pore structure evolution.

In the SSIDF framework, the feedback network is a physically grounded coupling system that links the three liquid-phase damage mechanisms—scaling, clay swelling, and water blocking through shared state variables (porosity φ and water saturation S_w). Each mechanism dynamically influences the others by altering these shared variables.

For instance, increased S_w due to water blocking reduces Darcy velocity u, which suppresses ionic diffusion and hence decreases the precipitation rate of scaling. Conversely, scale deposition raises local capillary pressure and enhances water retention, intensifying the water-blocking effect. Simultaneously, variations in ion concentration modify the membrane exchange coefficient ψ in the clay-swelling model, forming a bidirectional, closed-loop feedback among the three processes.

This network thus represents a nonlinear physical feedback system, rather than a data-driven neural network, and enables dynamic two-way interaction among the liquid-phase submodels.

(1) Feedback of water blocking on scaling reactions

In conventional inorganic scaling models, the precipitation reaction term is primarily controlled by ion concentration, without considering the influence of local hydrodynamic variations on reaction transport processes. In reality, the water blocking effect significantly increases water saturation in the near-wellbore region, leading to a reduction in Darcy velocity u, which inhibits both solute diffusion and convective transport, thereby suppressing effective precipitation reactions.

To account for this effect, we apply a hydrodynamic correction to the precipitation rate constant k_i and define the effective rate k_i^eff as in Eq. (38), where u_ref is the local Darcy velocity representing the characteristic scale of reactive transport in the low-velocity limit. This formulation captures the kinetic retardation induced by enhanced water-blocking.

$$k_i^\mathrm{eff} = k_i \frac{u}{u + u_\mathrm{ref}} \tag{38}$$

The hydrodynamic feedback expressed in Eq. (38) is physically and experimentally supported. Laboratory core-flood studies have repeatedly shown that higher flow velocities reduce the residence time of supersaturated brine near rock surfaces, thereby decreasing the local degree of supersaturation and the likelihood of mineral precipitation.

Khormali et al. (2016) demonstrated that calcium-carbonate scale deposition in core systems is strongly suppressed when the injection rate increases. Similarly, Azizi et al. (2019) reported that scale formation and particle retention diminish with increasing flow rate owing to enhanced mass-transfer and shear removal of nascent precipitates. Core-flood experiments for reactive-fluid transport (Ott et al., 2012) further confirmed that velocity-controlled reaction regimes exist in porous media.

Accordingly, the ratio $\frac{u}{u+u_\mathrm{ref}}$ in Eq. (38) serves as a normalized hydrodynamic damping factor capturing the experimentally observed inverse relationship between flow velocity and precipitation rate. The reference velocity u_ref is calibrated from core-flood data to reproduce the transition between reaction-limited and transport-limited regimes. This feedback term is physically consistent with previous thermo-hydro-mechanical and filtration-coupling studies on drilling-fluid invasion and mudcake evolution, which demonstrated that flow-velocity-dependent hydrodynamic feedback and dynamic boundary effects significantly affect near-wellbore transport processes (Ma et al., 2020; Peng et al., 2021, 2025). The model reproduces the same qualitative trend observed in these experiments—higher injection rate leading to weaker scaling-induced permeability loss (see Section 5.2)—thus confirming the physical validity of the feedback mechanism.

(2) Feedback of scaling on water blocking

Scale deposition markedly alters reservoir pore structure, increasing water retention volume and elevating capillary pressure, thereby raising saturation and aggravating water blocking. This effect is naturally incorporated into the permeability function of the water blocking model (Eq. (33)). In this work, the porosity evolution induced by precipitation is explicitly embedded into the relative permeability function of the water blocking model to implement this feedback pathway.

(3) Coupling between water blocking and clay swelling

Clay swelling damage is driven by the penetration–adsorption behavior of water molecules at the rock–pore interface. This process is not only influenced by salinity but also strongly affected by local hydrodynamics. In high water-blocking regions, although water saturation is high, the low flow velocity and limited effective diffusion pathways may suppress the entry of free water into interlayer structures. Therefore, in this study, the membrane mass exchange coefficient is no longer treated as an empirical constant. Instead, fluid–pore flux is introduced as a physical control variable, modifying the coefficient as follows:

$$\psi = \frac{J_\mathrm{w}}{J_\mathrm{w} + J_\mathrm{crit}} D^{\frac{2}{3}} \left(\frac{1}{\mu}\right)^{\frac{1}{3}} \left(\frac{1}{r_\mathrm{m}\kappa}\right)^{\frac{2}{3}} \left[1 - \frac{2I_1(r_\mathrm{m}\kappa)}{r_\mathrm{m}\kappa I_0(r_\mathrm{m}\kappa)}\right]^{\frac{1}{3}} \tag{39}$$

where $J_\mathrm{w} = uS_\mathrm{w}$ is the local water flux, and J_crit is the interfacial adsorption threshold under steady-state conditions, reflecting the limiting response of clay interlayers to water flux. This newly corrected membrane exchange coefficient characterizes swelling capacity under varying flow conditions and captures the behavioral trend of “rapid early swelling–later stabilization and convergence.”

(4) Implementation of the feedback loop

Within each time step t_n, the following iterative procedure is adopted:

① Solve the hydrodynamic field u, water saturation S_w, and ion concentration C_i;
② Evaluate the saturation index I_s to activate the scaling reaction term;
③ Update the membrane mass exchange coefficient ψ in the swelling model;
④ Update porosity φ, effective reaction rate k_i^eff, and permeability;
⑤ If the variable updates do not satisfy the convergence criterion, return to Step ①.

This strongly coupled three-mechanism model achieves a complete representation of the interactive evolutionary features of liquid-phase damage during drilling and completion by iteratively sharing and updating multiphysics variables spanning flow, chemistry, and mechanics. The above iterative steps constitute the computational realization of the feedback network. Within each global time step, the solver exchanges updated state variables among the three submodules until all field variables (u, S_w, C_i, ψ, and φ) satisfy the convergence criterion ($\|\Delta\varphi\|/\varphi_0 < 10^{-5}$). This ensures energy-consistent coupling and numerical stability. Compared with conventional sequential coupling, the feedback-network formulation maintains physical causality and eliminates artificial time-lag effects, allowing the SSIDF model to capture the nonlinear synergy among scaling, swelling, and water-blocking mechanisms in real time.

3.3. *Multimechanism coupling model: unified damage function based on SSIDF*

In engineering practice, indicators such as skin factor and permeability damage rate are commonly used to assess reservoir damage. However, these typically rely on linear summation or empirical formula combinations of different mechanisms, which fail to reveal the nonlinear responses and coupling feedbacks under the synergistic effect of multiple mechanisms. Section 2 have separately established coupling models for solid-phase and liquid-phase damage mechanisms, encompassing shared state variables such as permeability, porosity, and saturation. Building upon this, this study introduces the SSIDF, driven by structural disturbance. SSIDF integrates the outputs of multiple mechanisms and constructs a continuous mapping path of “mechanism-driven—structural response—macroscopic damage”, breaking away from the traditional model's separate accumulation paradigm.

The common outcome of various reservoir damage mechanisms is the evolution of effective flow channels, i.e., pore structure. Whether it is solid-phase particle blockage, inorganic scale deposition, clay swelling, or water blocking, the ultimate result can be viewed as a disturbance to local porosity. The total porosity can be expressed as the weighted summation of disturbances from each mechanism:

$$\varphi(\boldsymbol{r},t) = \varphi_0 - \sum_{i=1}^{n} w_i(\boldsymbol{r},t)\cdot\delta\varphi_i(\boldsymbol{r},t) \tag{40}$$

Starting from Kozeny-Carman, the intrinsic permeability scales as $K \propto \varphi^3/(\tau^2 S_\mathrm{v}^2)$, where φ is porosity, τ tortuosity, and S_v is the specific surface per unit volume. Empirical/PNM studies commonly represent τ by $\tau \propto \varphi^{-\alpha}$ with $\alpha \in [0, 1]$, and the morphology factor by $S_\mathrm{v} \propto (1-\varphi)^\beta$ with small β for weak texture evolution. Combining these gives an effective power-law sensitivity.

$$K \propto \varphi^{3+2\alpha}(1-\varphi)^{-2\beta} \tag{41}$$

For moderate $\delta\varphi$ about φ_0, the mapping from a normalized porosity disturbance $\overline{\delta_i} = \delta\varphi_i/\varphi_0$ to the permeability ratio can be locally approximated by

$$\frac{K}{K_0} \approx (1-\overline{\delta})^{\gamma_\mathrm{d}}, \gamma_\mathrm{d} \approx 3 + 2\alpha \,(\text{for } \beta \approx 0) \tag{42}$$

Because $\alpha \in [0,1]$ captures the observed variation from coarse, weakly tortuous media to finer, more tortuous frameworks, the corresponding exponent naturally falls in the bracket $\gamma_\mathrm{d} \in [2,5]$ when evaluated around realistic φ_0 and accounting for modest morphology effects. Eq. (43) therefore instantiates this mechanism-anchored power-law as the SSIDF permeability update.

$$K_\mathrm{d}(\boldsymbol{r},t) = 1 - \left[1 - \sum_i w_i(\boldsymbol{r},t)\cdot\overline{\delta}_i(\boldsymbol{r},t)\right]^{\gamma_\mathrm{d}} \tag{43}$$

where $\gamma_\mathrm{d} \in [2, 5]$ represents the nonlinear amplification degree of permeability due to porosity evolution, and $\overline{\delta_i} = \delta\varphi_i/\varphi_0$ is the normalized porosity disturbance rate. The SSIDF model naturally receives the structural disturbance variables output from the mechanism models in Section 2, as detailed in Table 3. The entire initial–boundary value problem for the multimechanism coupling model is shown in Table 4.

Compared to traditional linear summation models and product models, the SSIDF model offers the following advantages: structural rationality:

Table 3
Calculation methods for porosity disturbances under different mechanisms.

Mechanism type	Corresponding disturbance term calculation method ($\delta\varphi_i$)
Solid-phase damage (invasion + migration)	Obtained by integrating the precipitation concentration
Inorganic scaling	Converted from the mass of ionic precipitates
Clay swelling	Porosity compression induced by water diffusion/exchange
Water blocking effect	Local pore closure ratio caused by enhanced water saturation

Table 4
Initial–boundary value problem (IBVP) for the coupled multi-mechanism damage model.

Component	Governing equations	Initial condition	Boundary condition	Physical description
Solid-phase invasion	Eqs. (1, 2, 9–12)	$C(\boldsymbol{r},0) = C_d(\boldsymbol{r},0) = 0$	$C=\beta C_0$ at Γ_{in}, $C=0$ at Γ_{out}, $P=P_{in}$ at Γ_{in}, $P=P_{out}$ at Γ_{out}	Particle transport and deposition
Particle migration	Eqs. (1, 2, 9, 10, 12, 18 and 19)	$C(\boldsymbol{r},0) = C_d(\boldsymbol{r},0) = 0$	$C=0$ at Γ_{in}, $C=0$ at Γ_{out}, $P=P_{in}$ at Γ_{in}, $P=P_{out}$ at Γ_{out}	Internal particle mobilization
Inorganic scaling	Eqs. (9, 21–25)	$C_i(\boldsymbol{r},0) = C_{Formation}$	$C_i = C_{Liquid}$ at Γ_{in}, $P=P_{in}$ at Γ_{in}, $P=P_{out}$ at Γ_{out}	Precipitation under supersaturation
Clay swelling	Eqs. (9, 20, 21, 28 and 29)	$\varphi(\boldsymbol{r},0) = \varphi_0$, $c_1(\boldsymbol{r},0) = \varphi_0 S_{wc}$	$c_1 = \varphi_0$ at Γ_{in}, $P=P_{in}$ at Γ_{in}, $P=P_{out}$ at Γ_{out}	Diffusion-driven interlayer expansion
Water blocking	Eqs. (9, 20, 21, 33)	$u(\boldsymbol{r},0) = 0$, $S_w(\boldsymbol{r},0) = S_{wc}$	$P=P_{in}$ at Γ_{in}, $P=P_{out}$ at Γ_{out}	Capillary saturation growth
Coupled framework	Eqs. (36, 38–41)	$C_i(\boldsymbol{r},0) = C_{Formation}$, $\varphi(\boldsymbol{r},0) = \varphi_0$, $c_1(\boldsymbol{r},0) = \varphi_0 \cdot S_{wc}$, $u(\boldsymbol{r},0) = 0$, $S_w(\boldsymbol{r},0) = S_{wc}$	$C_i = C_{Liquid}$ at Γ_{in}, $c_1 = \varphi_0$ at Γ_{in}, $P=P_{in}$ at Γ_{in}, $P=P_{out}$ at Γ_{out}	SSIDF

- Based on a unified physical foundation with pore structure as the coupling intermediary.
- Strong mechanistic interpretability: Each disturbance corresponds to a physical effect of a mechanism, with each model coupling term mapping directly to the mechanism.
- Nonlinear response capture: The exponent γ captures the marginal amplification or saturation effects between mechanisms.
- Ease of expansion and integration: New mechanism disturbance terms, such as wettability reversal or bacterial blockage damage that may occur in later stages (e.g., during waterflooding), can be easily incorporated.

3.4. *Model limitations and potential deviations due to simplification of scaling kinetics*

It should be noted that the present inorganic scaling model adopts a single-rate reaction formulation activated by the saturation index, which simplifies the complex multicomponent precipitation processes occurring in real formation water systems. This simplification neglects potential interactions among multiple mineral species (e.g., Ca–Ba–Sr sulfates or mixed carbonate–sulfate systems), temperature–pressure coupling effects on reaction kinetics, and variations in precipitate crystal morphology. Such factors may cause deviations in the predicted scaling intensity or spatial distribution, particularly in reservoirs with strong chemical heterogeneity or high ionic strength.

Nevertheless, for the targeted near-wellbore conditions considered in this study—where ionic composition and thermodynamic conditions remain relatively stable within a limited radial domain—the single-rate approach provides an acceptable first-order approximation and maintains numerical tractability and stability. Future work will incorporate multi-mineral co-precipitation kinetics and temperature–pressure coupling into the SSIDF framework to enhance its general applicability under more complex geochemical conditions.

4. Numerical implementation and verification

4.1. *Semi–implicit finite–difference scheme*

The governing equations described above were discretized using a semi–implicit finite–difference scheme to ensure stability and efficiency in solving the coupled nonlinear system. The scheme combines explicit treatment of nonlinear reaction terms with implicit updating of diffusion and coupling terms, thus enabling larger time steps without compromising numerical stability. The spatial domain was discretized using logarithmic grid spacing to capture steep gradients near the wellbore, while maintaining computational efficiency in the far–field. A detailed derivation of the discretization and coordinate transformation can be found in Appendix B.

To validate the numerical accuracy, grid refinement tests were conducted to verify mesh independence and to quantify the discretization error using RMSE and L_2 norms. Furthermore, the semi-implicit scheme was evaluated for numerical stability and convergence under refined temporal and spatial resolutions. The verification results are presented in Sections 4.2 and 4.3, confirming that the proposed scheme achieves second–order spatial accuracy and unconditional stability within the parameter range of interest.

4.2. *Grid independence and RMSE evaluation*

To examine the mesh independence and spatial accuracy of the semi-implicit finite-difference model, simulations were performed with grid resolutions $n_x = 4, 8, \ldots, 1024$ while keeping the time step constant at $\Delta t = 0.1$. The root mean square error (RMSE) and the L_2 and L_∞ norms of the permeability-damage profile $K_d(r)$ were computed with respect to the finest grid ($n_x = 1024$) reference.

As summarized in Table 5, the RMSE decreases steadily from 2.84×10^{-1} at $n_x = 4$ to 1.01×10^{-3} at $n_x = 512$. The L_2 and L_∞ norms show the same monotonic decline, indicating that the solution becomes effectively grid-independent when $n_x \geq 256$.

As shown in Fig. 8, a least-squares regression of log(RMSE) against log(h) using all non–zero errors gives an empirical slope $p = 1.13$, confirming first-order spatial accuracy. This order is consistent with the upwind discretization of the advective term, which governs the overall truncation error even though the diffusion operator itself is second order.

Table 5
Grid-independence and RMSE evaluation.

n_x	RMSE	L_2	L_∞
4	2.84×10^{-1}	9.08	4.23×10^{-1}
8	1.38×10^{-1}	4.43	1.99×10^{-1}
16	6.63×10^{-1}	2.12	9.48×10^{-2}
32	3.19×10^{-2}	1.02	4.56×10^{-2}
64	1.53×10^{-2}	0.49	2.18×10^{-2}
128	7.09×10^{-2}	0.23	1.01×10^{-2}
256	3.03×10^{-2}	0.097	4.32×10^{-3}
512	1.01×10^{-3}	0.032	1.44×10^{-3}

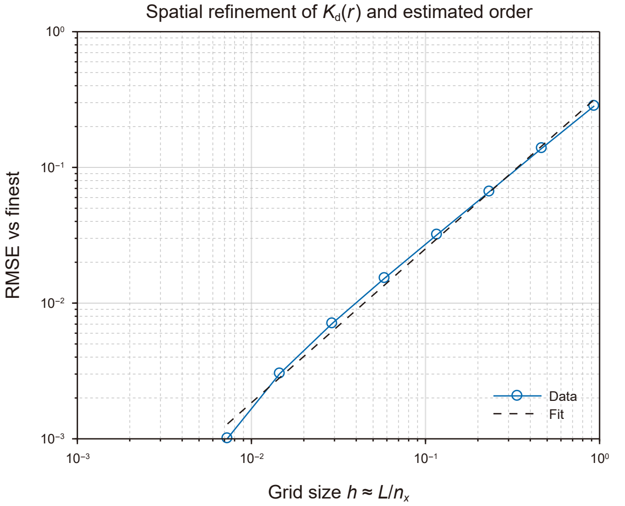

Fig. 8. Log-log plot of RMSE versus grid size h. The regression slope $p \approx 1.13$ confirms first-order spatial accuracy and grid independence for $n_x \geq 256$.

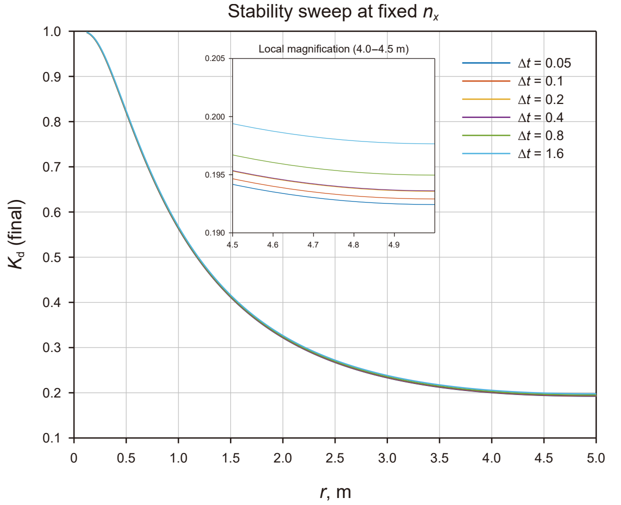

Fig. 9. Stability sweep of the semi-implicit scheme at fixed $n_x = 400$. The overlapping $K_d(r)$ profiles for time steps $\Delta t = 0.05$–1.6 indicate first-order temporal accuracy and strong numerical stability.

4.3. Stability and convergence analysis

Temporal-refinement and stability tests were conducted at a fixed spatial resolution of $n_x = 400$. Time steps were reduced successively from $\Delta t = 25.6$ to 0.025. The RMSE of $K_d(r)$ decreases monotonically from 7.71×10^{-2} at $\Delta t = 25.6$ to 6.34×10^{-5} at $\Delta t = 0.05$ (Table 6). A least-squares regression of log(RMSE) versus log(Δt) gives an empirical slope $p_t = 1.06$, verifying first-order temporal accuracy. This result is consistent with the backward–Euler time integration employed in the semi-implicit scheme.

A stability sweep covering $\Delta t = 0.05$–1.6 was also performed. As shown in Fig. 9, all computed $K_d(r)$ curves for different Δt values almost overlap, showing no oscillation or divergence. This demonstrates that the proposed semi-implicit method maintains strong numerical stability and behaves as effectively unconditionally stable over the parameter range investigated.

4.4. Parameter sensitivity and uncertainty quantification

To evaluate the robustness of the SSIDF framework, a global sensitivity and uncertainty analysis was conducted using Latin hypercube sampling (LHS) of three empirical parameters: the deposition coefficient k_i^{eff}, the particle–fluid interaction factor γ, and the formation property factor ψ. One hundred samples were generated within physically realistic ranges ($k_i^{\text{eff}} \in [10^{-4}, 10^{-1}]$ log–uniform; $\gamma_d \in [2, 5]$; $\psi \in [0.1, 0.7]$). Each sample was evaluated under identical spatial and temporal discretization ($n_x = 400$, $\Delta t = 0.1$, $t_{\text{end}} = 200$). Standardized regression coefficients (SRC) and rank-SRC were computed between inputs and four key outputs—near-wellbore damage $K_d(r_w)$, domain-averaged damage $\overline{K_d}$, maximum damage K_{dmax}, and the skin factor S. The results are summarized in Table 7 and Fig. 10. Both SRC and rank-SRC reveal consistent trends.

The deposition coefficient k_i^{eff} dominates all damage indicators (|SRC|> 0.75), confirming its primary role in controlling the rate and magnitude of particle deposition. ψ shows a secondary but non-negligible effect (|SRC|≈ 0.35–0.50), particularly influencing averaged quantities and skin factor, whereas the particle–fluid interaction factor γ_d exerts only a moderate influence (|SRC|< 0.35). No sign of numerical instability or non-monotonic behavior was observed across the parameter space, demonstrating that the semi-implicit solver remains robust to substantial parameter perturbations.

While the present analysis focuses on deterministic calibration and variance-based sensitivity using LHS-SRC, the same framework can be extended to full uncertainty quantification (UQ) using Sobol indices or probabilistic surrogate models such as the deep energy method (DEM), enabling uncertainty-aware formation-damage prediction in future work.

Table 6
Temporal convergence and stability verification.

Δt	RMSE	L_2	L_∞
25.6	7.71×10^{-2}	1.54	9.95×10^{-2}
12.8	4.58×10^{-2}	0.92	5.89×10^{-2}
6.4	2.99×10^{-2}	0.60	3.88×10^{-2}
3.2	1.27×10^{-2}	0.25	1.62×10^{-2}
1.6	3.99×10^{-3}	0.080	5.31×10^{-3}
0.8	1.96×10^{-3}	0.039	2.62×10^{-3}
0.4	9.51×10^{-4}	0.019	1.27×10^{-3}
0.2	1.03×10^{-3}	0.021	1.34×10^{-3}
0.1	4.83×10^{-4}	0.0097	6.34×10^{-4}
0.05	6.34×10^{-5}	0.00127	8.46×10^{-5}

5. Nonlinear synergistic effects of multimechanism reservoir damage

In this study, five types of damage mechanisms are modeled based on the radial diffusion-convection-reaction control equations, and numerical solutions are obtained using a semi-implicit finite difference method on the MATLAB platform. Considering the significant variations in permeability and concentration in the near-wellbore region, the model adopts a logarithmic coordinate transformation $r = r_w e^x$, as detailed in Appendix B. Building upon

Table 7
Standardized regression coefficients (SRC) and rank-SRC for key outputs.

Parameter	$K_d(r_w)$	$\overline{K}_d$	K_{dmax}	S
k_i^{eff}	−0.88 (−0.92)	−0.77 (−0.89)	−0.77 (−0.85)	+0.74 (+0.82)
γ_d	+0.18 (+0.24)	+0.25 (+0.27)	+0.33 (+0.37)	−0.22 (−0.22)
ψ	−0.26 (−0.30)	−0.38 (−0.38)	−0.37 (−0.38)	+0.50 (+0.52)

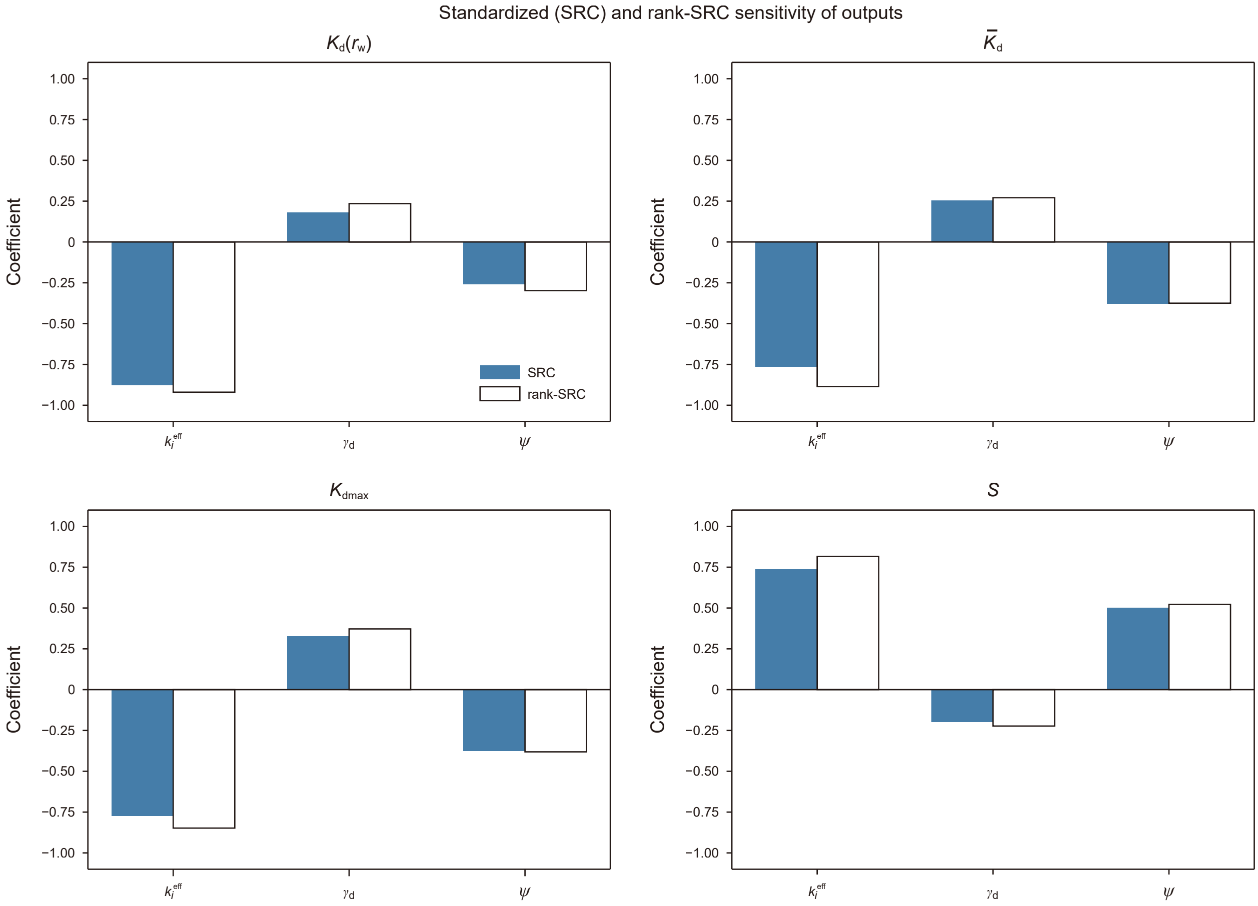

Fig. 10. Bar plots of SRC values for the four model outputs.

this, a nonlinear synergistic effect analysis of multimechanism reservoir damage is conducted.

5.1. Nonlinear synergistic analysis of solid-phase damage

Pressure is the driving force for solid particle deposition and migration. Therefore, considering the initial permeability of 450 × 10^{-3} μm^2, initial porosity of 18%, and different pressure differentials, the evolution of skin factor over time is calculated using the solid-phase coupling model, simple summation model, and single-factor damage model, as shown in Fig. 11.

As shown in Fig. 11(a), on the 50th day, when the pressure differential is 1.5 MPa, the total skin factor considering solid-phase coupling is 0.2066 lower than that of the non-coupled model, with results being quite similar. As the pressure differential approaches zero (i.e., less than 1.5 MPa), the results of both models will converge. This suggests that when the pressure differential, a driving factor, is small, the coupling between mechanisms and the independent summation of individual damages can be considered negligible. Under very low pressure differential conditions, particle migration is limited, and the interactions between solid-phase damage mechanisms are weak, making the assumption of their independence highly reasonable. At this point, the total damage is minimal, and changes in rock permeability and pore structure are negligible. Meanwhile, the particle concentration is very low, and the probability of particle interactions or interference is minimal, so the coupling effects between mechanisms are insignificant.

At pressure differentials of 2 and 3.6 MPa, the total skin factor on day 50 for the coupled model is 0.2637 and 0.2862 lower than that of the non-coupled model (Fig. 11(b) and (c)), showing that their interaction has a significant suppressive effect on total damage. This indicates that under high-pressure differential conditions, the concentration of particles in the medium increases, enhancing particle collisions and interference, which leads to significant interactions between damage mechanisms. The coupling effects must be considered. However, the increase in skin factor from 2 to 3.6 MPa is much smaller than that from 1.5 to 2 MPa. This is because the invading solid-phase particles reduce the reservoir's instantaneous permeability, thereby weakening the migration ability of particles. Meanwhile, migrating particles also hinder the subsequent invasion of solid-phase particles to some extent, forming a bidirectional limiting effect.

Under the same input conditions as in Fig. 10, when the initial porosity is varied, the results are shown in Fig. 12. As shown in Fig. 12(d–f), the porosity of the reservoir significantly affects the evolution rate of solid-phase damage. The evolution of the skin factor indicates that reservoirs with high porosity not only have faster initial damage growth rates but also a longer duration of continuous growth, reflecting a stronger cumulative clogging ability. This phenomenon aligns with physical intuition: in low-porosity media, pore throat channels have certain screening and blocking capabilities, preventing deep migration of foreign particles, leading to a relatively confined and rapid saturation of damage patterns.

From Fig. 12(a–c), it can be observed that under low porosity conditions, the narrow channels allow only very fine particles to pass through, and foreign solid-phase particles are trapped early in the near-zone, making particle migration the primary solid-phase

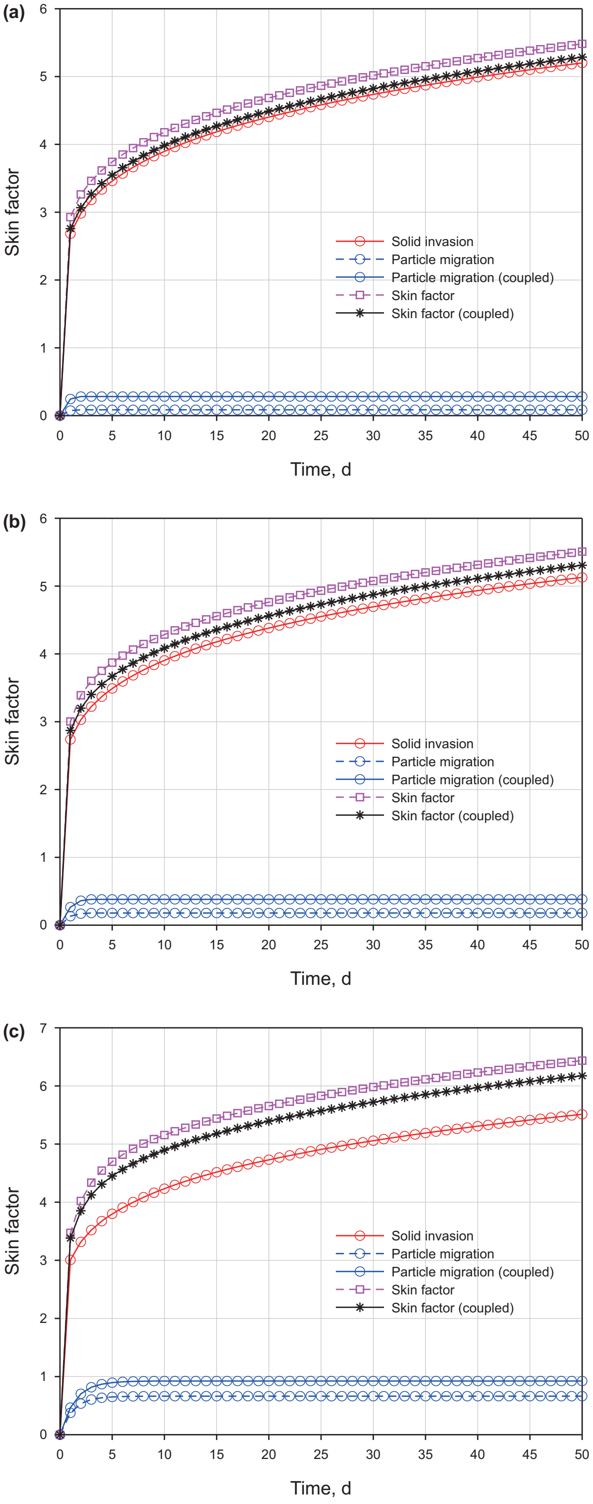

Fig. 11. Comparison of solid-phase coupling model, simple superposition model, and single-factor damage results under different pressure differentials: (**a**) 1.5 MPa, (**b**) 2.0 MPa, (**c**) 3.6 MPa.

damage mechanism. In contrast, Fig. 12(d–f) show that under high porosity conditions, the channels are large enough for most foreign particles to penetrate directly, reducing the shear flow rate in the later stages and inhibiting particle migration, manifesting as solid-phase invasion-dominated “single-type” damage. Under medium porosity conditions, both particle invasion and particle detachment migration can occur in certain regions simultaneously, displaying clear coupling characteristics (Fig. 12(e)).

5.2. Nonlinear synergistic analysis of liquid-phase damage

Since liquid-phase damage mechanisms share the porosity variable, this section examines the differences between the liquid-phase coupling model and other models under formation water salinity of 24,237.2 mg/L, invading fluid salinity of 48,359.3 mg/L, clay content of 10%, and varying porosity conditions. The first comparison involves the results of the unidirectional coupling model for inorganic scaling and clay swelling versus single-factor damage models, as shown in Fig. 13.

From Fig. 13(a–c), it can be observed that as initial porosity decreases, the total damage becomes more severe. Under identical conditions, the skin factor calculated by the clay swelling–inorganic scaling coupling model is consistently lower than that of the simple superposition model. This is mainly because the coupling model incorporates the inhibitory effect of salinity on clay swelling, thereby reducing permeability loss caused by swelling. Fig. 13(d) shows that the unidirectional coupling model successfully captures the nonlinear enhancement of inorganic scaling damage as porosity decreases—that is, the smaller the porosity, the larger the proportion of pore space occupied by small-scale precipitate blockages. However, because the unidirectional coupling model does not account for the coupling effects of water blocking with the other two mechanisms, the overall damage trend is relatively simple, reflecting only the mutual inhibition between clay swelling and inorganic scaling.

With porosity fixed at 10% and the same input parameters as in Fig. 13, the liquid-phase three-mechanism coupling model (true coupling, shown in Fig. 14) and the aforementioned unidirectional coupling model (placeholder coupling, also shown in Fig. 14) are compared under different initial water saturations and clay mineral contents. Fig. 14(a) shows that the water-blocking skin factor in the three-mechanism coupling model is 2.798, which is higher than any of the water-blocking skin factors in Fig. 13, and exceeds the contribution of clay swelling. This result is more consistent with physical intuition, since lower porosity is usually accompanied by smaller pore throat radii and higher capillary pressures, thereby intensifying water retention effects and making water blocking damage more significant.

In Fig. 14(b), when clay mineral content is increased to 50%, the average swelling rate of clay hydration rises to 2.92 times its original value, providing a good explanation for the positive feedback in clay-rich reservoirs: water blocking supplies bound water, which reinforces clay swelling. During the hydration of clay minerals (e.g., montmorillonite), bound water—especially capillary water—serves as a critical medium for the hydration reaction, facilitating interlayer expansion. Bound water is also often enriched with ions that participate in interlayer cation exchange, a key mechanism of swelling.

Fig. 14(c) and (d) show that as initial water saturation increases from 5% to 15%, water presence continues to promote swelling under the unidirectional coupling mechanism. However, in Fig. 14(d), the time required for the three-mechanism coupling model’s total skin factor to exceed that of the simple superposition model is significantly delayed. This validates the physical reality that “a moderate amount of water accelerates clay swelling, while excessive water dilutes ion concentration, thereby inhibiting cation exchange and slowing the swelling rate.

5.3. Spatiotemporal evolution of multimechanism reservoir damage

The total reservoir damage throughout the drilling and completion process, with an initial permeability of 450 × 10^{-3} μm^2,

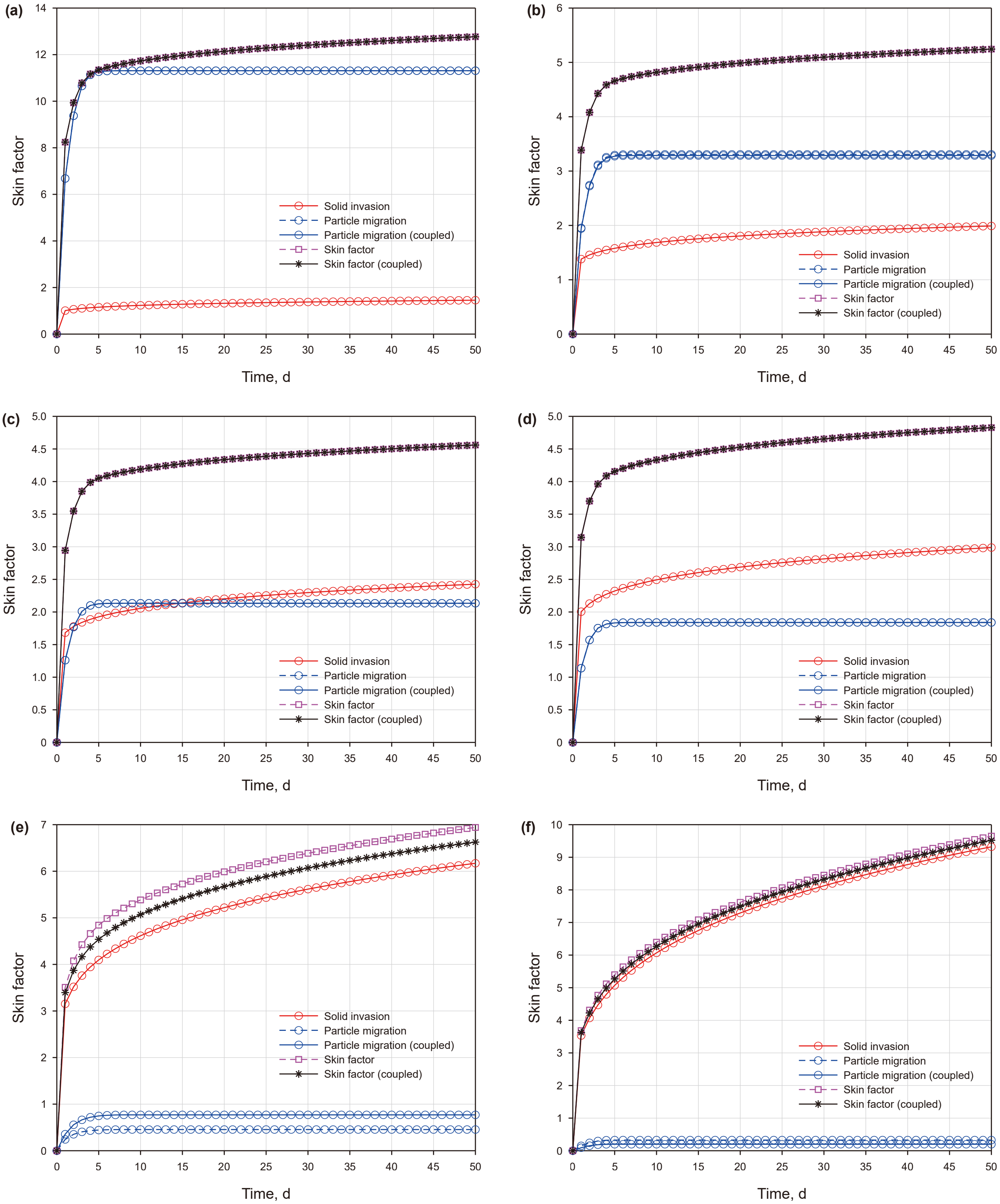

Fig. 12. Comparison of solid-phase coupling model, simple superposition model, and single-factor damage results at different initial porosities: (**a**) 5%, (**b**) 7%, (**c**) 9%, (**d**) 10%, (**e**) 20%, (**f**) 30%.

initial porosity of 18%, formation water salinity of 24,237.2 mg/L, invading fluid salinity of 48,359.3 mg/L, and clay content of 10%, is characterized using the SSIDF model. The results are presented as real-time permeability changes, as shown in Fig. 15. Damage caused by the drilling and completion fluid typically exhibits a "wellbore-centered, radially decreasing" spatial distribution, which aligns with the spatiotemporal evolution of real-time permeability shown in Fig. 15: the closer to the wellbore and the longer the exposure time, the lower the permeability.

Fig. 16 further illustrates the spatial distribution changes of real-time permeability at different time points, with the wellbore located at the center (0.12 m). As shown in Fig. 16(a) and (e), by Day

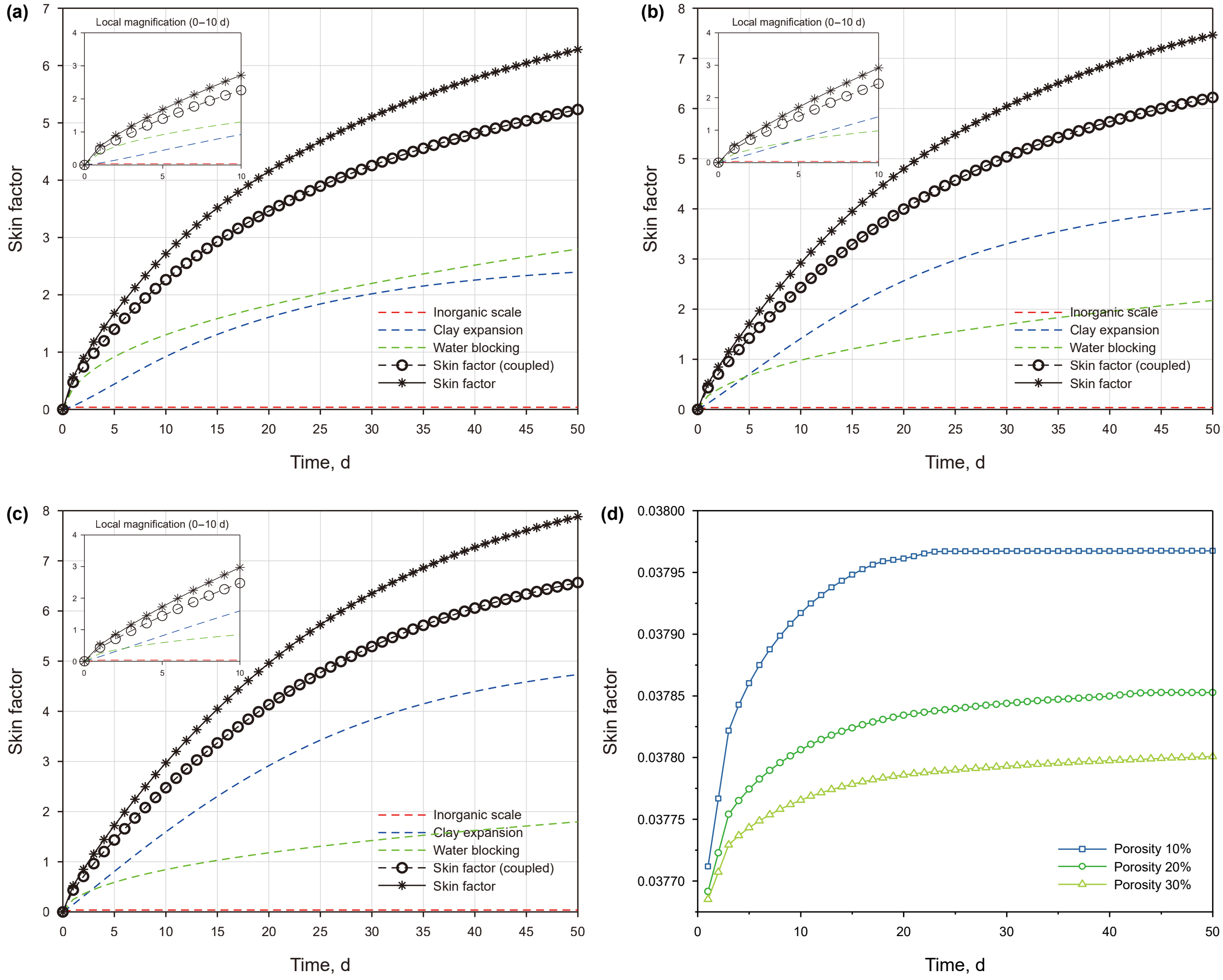

Fig. 13. Results of unidirectional coupling model and single-factor damage model under different porosities: (**a**) porosity 10%, (**b**) porosity 20%, (**c**) porosity 30%, (**d**) inorganic scaling damage under three porosities.

11.20, noticeable damage has already occurred around the wellbore. As the soaking time increases (Fig. 16(b–h)), the damage gradually penetrates deeper into the reservoir. In actual reservoirs, if the damage starts from the middle of the formation, a damage band with a Gaussian-like distribution will form. The part depicted in Fig. 16 represents the lower half of this damage zone, showing the heterogeneity of reservoir damage in spatial distribution. As seen in Fig. 16(h), as the pressure gradient decreases, filtrate invasion saturates, and reactant depletion occurs, the damage no longer extends rapidly into the reservoir around Day 65 but instead stabilizes.

In the near-wellbore region, solid-phase and liquid-phase invasions exhibit significant differences in their spatial distribution characteristics. This is mainly due to the fundamental differences in their migration mechanisms and their interaction with the reservoir medium. Solid-phase particles, which primarily come from bridging agents, weighting agents, and clay particles in the drilling or completion fluid, are migration-limited by pore throat size and screening effects. They typically form high-intensity damage zones within a 0.2–1.0 m range near the wellbore (Fig. 17(a)). In this region, particles are prone to deposition and retention, causing a sharp decrease in permeability, and exhibit a wellbore-centered, annular symmetric distribution pattern under homogeneous reservoir conditions.

In contrast, the invasion of liquid-phase filtrate is driven by both pressure differential and capillary forces, allowing it to significantly break through the solid-phase invasion front and migrate deeper into the reservoir, forming secondary damage zones. This liquid invasion typically extends 2–5 m beyond the wellbore (Fig. 17(b)), with the exact range depending on the formation's pore structure, fluid properties, and pressure conditions. Within this region, the filtrate can trigger various damage mechanisms, such as clay mineral clay swelling, water blocking effects, and inorganic scaling precipitation. Although the extent of damage is generally weaker than in the near-wellbore zone, its impact on the flow capacity remains significant. Consequently, a radial zoning structure forms around the well, with a primary damage zone dominated by solid-phase invasion and a secondary damage zone controlled by liquid-phase invasion (Fig. 17(c)).

5.4. Comparison with alternative frameworks

It is worth noting that advanced numerical and learning-based frameworks, such as the cracking particle method (CPM) (Rabczuk and Belytschko, 2004) and the deep energy method (DEM) (Wang et al., 2023), provide alternative paradigms for modeling complex coupled processes. CPM allows explicit representation of fracture evolution in solid mechanics through particle-based enrichment functions, making it ideal for problems dominated by structural

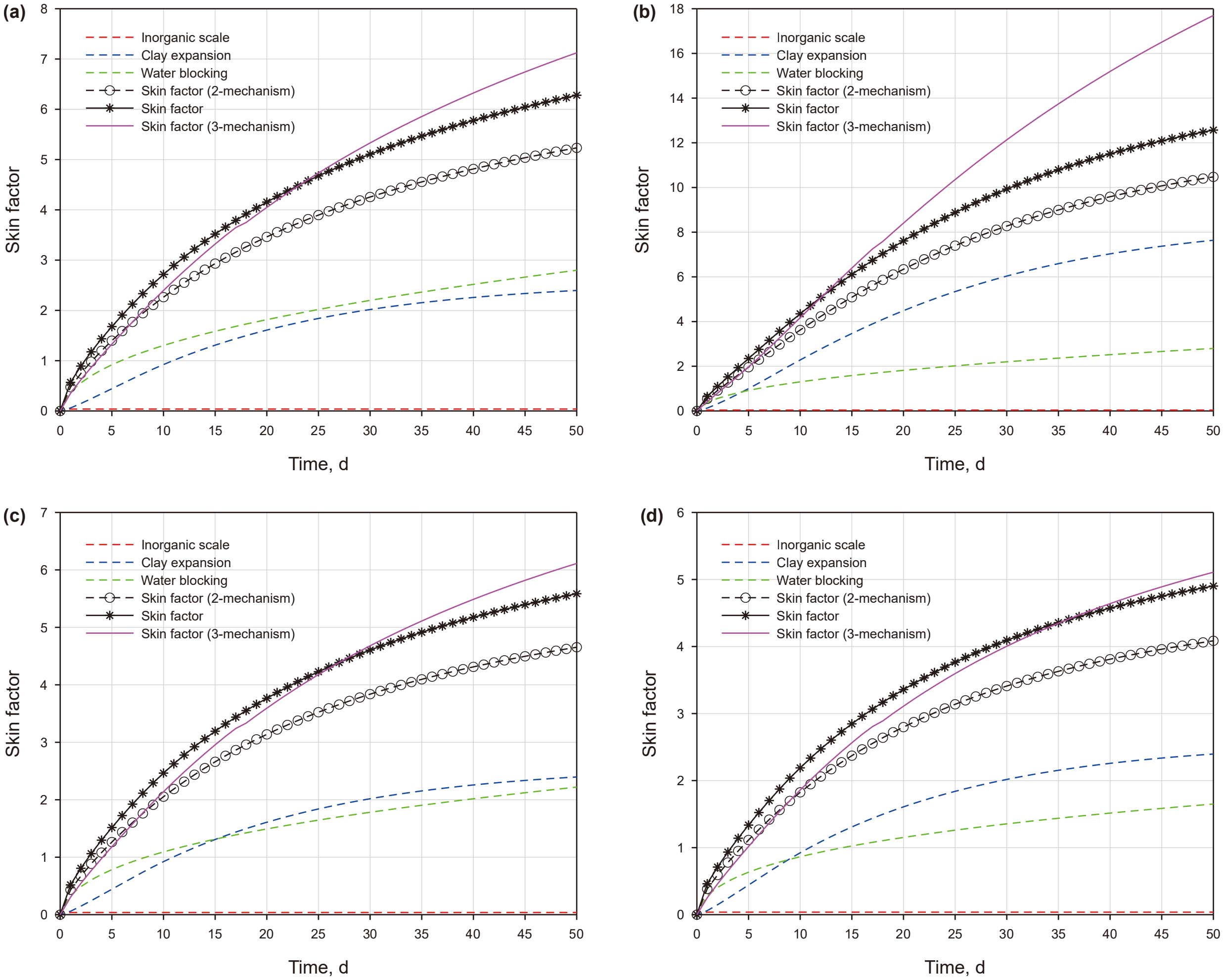

Fig. 14. Results of liquid-phase three-mechanism coupling model and unidirectional coupling model: (**a**) clay content 20%, initial water saturation 5%, (**b**) clay content 50%, initial water saturation 5%, (**c**) clay content 20%, initial water saturation 5%, (**d**) clay content 20%, initial water saturation 15%.

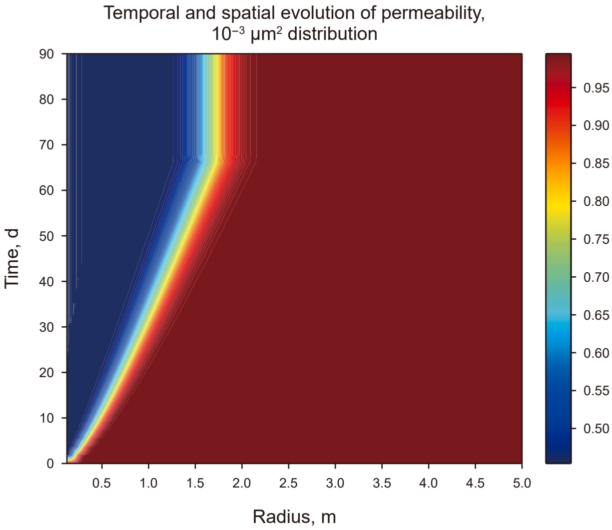

Fig. 15. Variation of real-time permeability with time and distance from the wellbore.

failure. In contrast, the DEM formulates physics-governed energy functionals and employs neural networks to solve both forward and inverse problems without discretization, naturally incorporating uncertainties and experimental data.

The SSIDF framework differs fundamentally from these approaches. Instead of replacing the governing equations with purely data-driven surrogates, it preserves mechanistic interpretability by explicitly coupling multiple physicochemical damage processes via shared state variables and a bidirectional feedback network. While DEM offers higher flexibility for inverse design, SSIDF provides clearer physical insight and stronger constraints on process-specific interactions, making it more suitable for practical formation damage analysis where mechanistic transparency and limited data availability are critical.

6. Field validation and application

The multimechanism reservoir damage coupling model developed in this study has been applied in field operations in oilfields such as Gudong and Zhanjiang. The applications include two aspects: (1) diagnosing existing damage in order to develop targeted reservoir damage prevention and remediation strategies; and (2) predicting potential damage to provide a theoretical basis for preventive measures. This section illustrates the applications with two field cases.

The two validation wells are located in geologically distinct regions of China. GO7 lies in the central Gudong Oilfield of the Shengli Basin, eastern China. The target interval is a Neogene Guantao sandstone at 2.9–3.1 km depth, consisting of fine-to

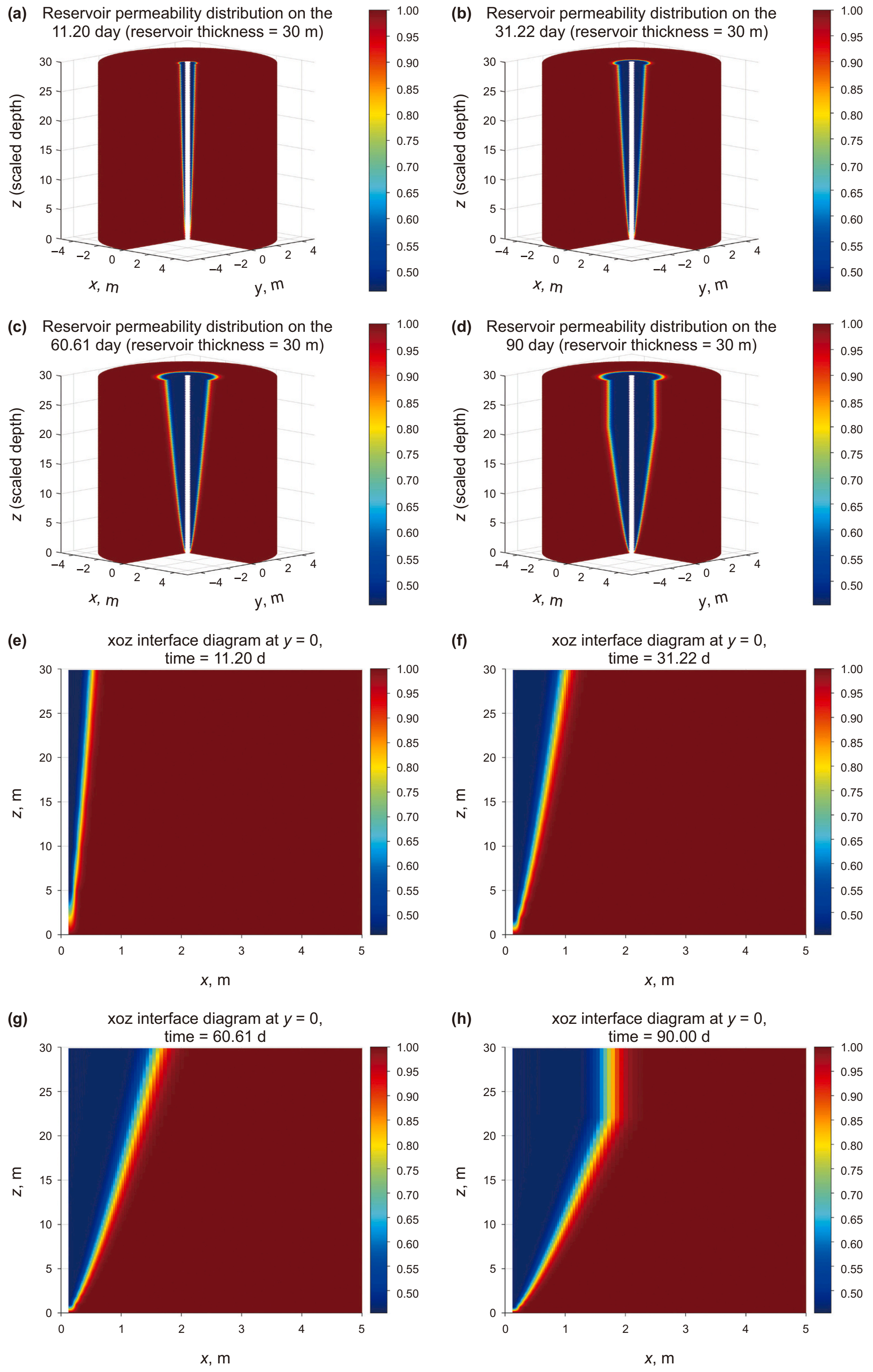

Fig. 16. Near-wellbore permeability distributions at different times: (**a**), (**e**) 11.20 days; (**b**), (**f**) 31.22 days; (**c**), (**g**) 60.61 days; (**d**), (**h**) 90.00 days.

medium-grained quartz–feldspar sandstones ($\varphi \approx$ 18%–21%, $K \approx$ 80–110 mD) containing ~35% illite and 25% kaolinite. YL8 is situated in the Songnan Low Uplift of the Qiongdongnan Basin, northern South China Sea. Its reservoir is a mid-Miocene marine sandstone at 2.7–2.9 km, with porosity 20%–23% and permeability 60–90 mD. The formation is more heterogeneous, with alternating siltstone interbeds and a higher clay fraction (~30%). Formation water salinity in both regions is 110–130 g/L (NaCl-$CaCl_2$ type). The

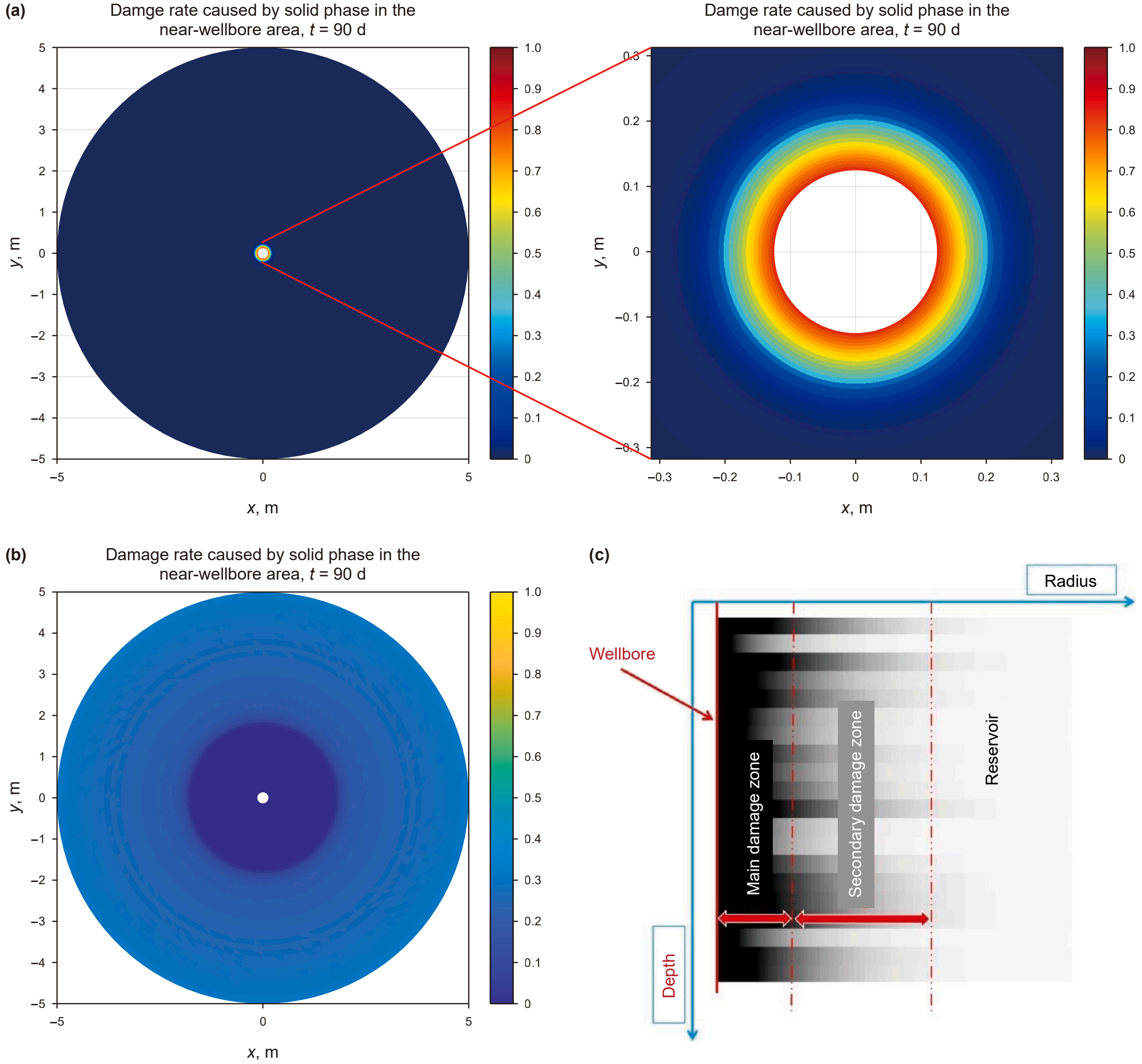

Fig. 17. Comparison of solid-phase and liquid-phase invasion depths: (**a**) spatial distribution of solid-phase damage, (**b**) spatial distribution of liquid-phase damage, (**c**) schematic diagram of the damage zone.

injected drilling/completion fluids are low-salinity (3–5 g/L) water-based muds containing polymeric filtrate reducers and KCl shale inhibitors. These data clarify the geological and operational contexts under which the SSIDF framework was validated.

For reference, the “traditional additive model” here refers to the direct linear summation of the five single-mechanism damages without any coupling or feedback among them.

6.1. Damage diagnosis

For Well GO7 in the Gudong Oilfield, calculations were performed using the input parameters provided in Appendix C.1, with results shown in Fig. 18. According to the methodology listed in Table 3, the contributions of various damage mechanisms were quantified. The completion fluid used in this well had a low solid content and relatively low salinity, with potassium chloride (KCl) solution as the main component. Consequently, the dominant damage mechanisms were water blocking and particle migration, while clay swelling, inorganic scaling, and solid-phase invasion were relatively minor (Fig. 18(b)). The coupled multi-mechanism reservoir damage model calculated a skin factor of 5.09 (Fig. 18(a)), compared with a measured skin factor of 5.16, whereas the simple superposition model yielded 5.65. The accuracy of the coupled model reached 98.64%, representing an 8.14% improvement in accuracy over the simple additive approach.

The model achieves a predictive accuracy of 98.6% for the validated field cases, reflecting its strong agreement with measured data under calibrated parameter conditions. It should be noted that this value represents the accuracy obtained within the available parameter and data range, and not an absolute measure applicable to all reservoirs. In practice, when parameter uncertainty is larger, the model maintains robust performance with a moderate sensitivity, as shown in Section 4.4.

Based on the diagnostic results, conventional mud acid combined with surfactants was applied for damage removal. As a result, daily oil production increased from 2.2 to 4.27 m^3/d, achieving a 94.09% increase in output.

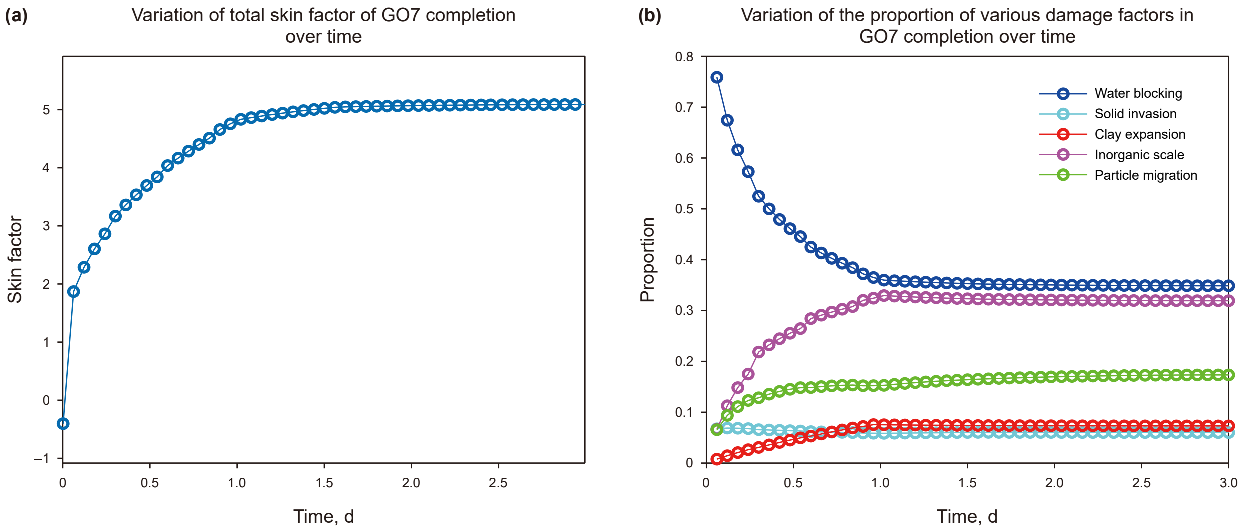

Fig. 18. Diagnostic results of Well GO7: (**a**) variation of calculated skin factor over time, (**b**) contribution of each damage mechanism over time.

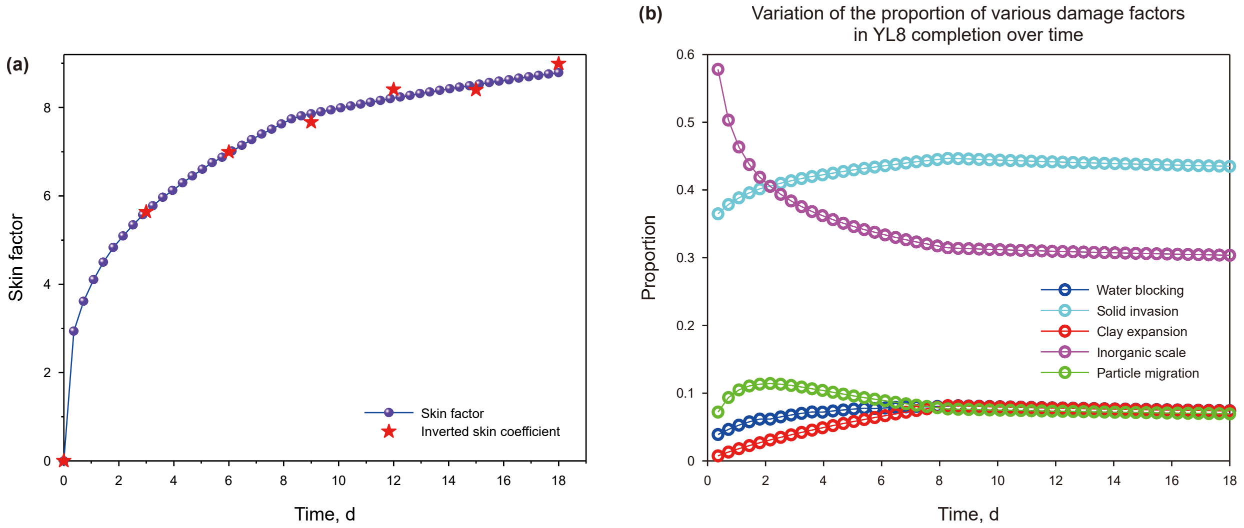

Fig. 19. Prediction results of Well YL8: (**a**) comparison between calculated and inversion results, (**b**) contribution of each damage mechanism over time.

6.2. Damage prediction

Well YL8 is a deepwater gas well. The skin factor back-calculated from the daily production data was compared with predictions from the multimechanism damage coupling model, as shown in Fig. 19(a). The mean absolute percentage error (MAPE) was approximately 1.46%, indicating that the accuracy of the multimechanism coupling model reached 98.54%. The drilling fluid in this well had both high solid content and high salinity, which suppressed clay mineral swelling almost completely, while inorganic scaling accounted for a large portion of the damage. In addition, the reservoir had relatively large average pore sizes, making solid-phase invasion the dominant damage mechanism. The calculated results were consistent with field observations.

7. Conclusions

(1) To address the multiphysical and multimechanism interferences that occur during drilling and completion, this study develops a unified damage modeling framework dominated by structural disturbance. The framework incorporates five mechanisms—solid-phase invasion, particle migration, water blocking, inorganic scaling, and clay swelling—thus breaking the traditional paradigm of “independent mechanisms and additive outcomes”.

(2) A unified damage factor function, SSIDF, is proposed, with pore structure disturbance as the central mediator. This function provides a unified characterization of the impact of different damage mechanisms on permeability evolution, offering strong physical interpretability and extensibility.

(3) A three-mechanism two-way feedback model—“scaling–swelling–water blocking”—is constructed to reveal the nonlinear synergistic interactions among liquid-phase damages. The model reflects the regulatory role of salinity, hydrodynamics, and pore parameters on the intensity of these interactions.

(4) Numerical simulations indicate that bidirectional restriction under solid-phase coupling significantly reduces the overall degree of damage, while liquid-phase mechanisms exhibit obvious amplification effects under medium- and low-

porosity conditions. The spatial distribution of damage demonstrates a typical annular structure consisting of a “primary damage zone + secondary damage zone”.

(5) Field validation was conducted in two typical wells in the Gudong and Zhanjiang Oilfields. The model achieved a skin factor prediction accuracy of up to 98.6%, effectively distinguishing the contributions and evolutionary trends of different damage mechanisms, thereby demonstrating strong field adaptability and application potential.

(6) The model is applicable for identifying the synergistic responses of complex damage mechanisms in various types of reservoirs. It shows excellent adaptability and foresight in scenarios such as sensitivity-induced damage in high-clay-content formations and compound damage triggered by strong temperature-pressure disturbances in deepwater reservoirs. The model thus provides a quantitative support tool for integrated drilling–completion design and damage control in unconventional oil and gas reservoirs.

(7) Future work will focus on extending the SSIDF framework to incorporate mechanical damage and fracture propagation using meshfree particle-based schemes such as CPM, and to explore hybrid energy-driven learning strategies inspired by the deep energy method for uncertainty quantification and inverse optimization.

CRediT authorship contribution statement

Ke-Ming Sheng: Writing – review & editing, Writing – original draft, Visualization, Software, Resources, Methodology, Formal analysis, Data curation, Conceptualization. **Guan-Cheng Jiang:** Supervision, Project administration, Funding acquisition. **Ming-Liang Du:** Writing – review & editing, Writing – original draft. **Lan Qiao:** Writing – review & editing. **Yin-Bo He:** Supervision, Resources, Formal analysis.

Data availability

All data is available from the manuscript and https://github.com/U2647/SSIDF.git.

Declaration of competing interest

The authors declare that they have no known competing financial interests or personal relationships that could have appeared to influence the work reported in this paper.

Acknowledgements

This work is financially supported by National Natural Science Foundation of China (No. U23B2082) and Oil & Gas Major Project (No. 2025ZD1404600). Ke-Ming Sheng was supported by the China Scholarship Council (202406440017) for one year research at the University of Dundee. We appreciate the editors and reviewers for their valuable and constructive comments and suggestions.

Notation

α	Vertical diffusion coefficient
α_0	Proportional constant
α_1	Time decay factor (s^{-1})
A_k	Temperature sensitivity factor
A_s	Geometric correction factor
β_1	Particle attachment efficiency, dimensionless
β_2	Time decay rate (m^{-1})
β_i, β_j	Reaction coefficients of the corresponding ions in reaction equations
c_0	Initial volumetric fraction of water in the rock solid phase
c_1	Dynamic volumetric fraction of water in pores at a given time
C	Volumetric concentration of solid phase in invading fluid, %
C_0	Volumetric concentration of solid phase in invading fluid, %
C_d	Volumetric concentration of deposited particles, %
C_{dmax}	Maximum deposition saturation, %
C_i	Concentration of ion *i*, mg/L
$[Cat]$、$[An]$	Concentrations of free cations and anions, respectively, mg/L
C_t	Comprehensive rock–fluid compressibility coefficient
$\delta\varphi_i$	Porosity disturbance induced by mechanism *I*
D	Diffusion coefficient of water molecules
D_g, D_p	Particle diameters, μm
Γ_{in}	Wellbore surface (inner boundary)
Γ_{out}	Reservoir boundary (outer boundary)
$I_0(x)$	Zeroth-order modified Bessel function of the first kind
$I_1(x)$	First-order modified Bessel function of the first kind
I_s	Saturation coefficient
k	Filtration coefficient
k_i	Precipitation reaction rate constant of ion *i*
k_{i_0}	Initial precipitation reaction rate constant of ion *i*
k_B	Boltzmann constant
K	Instantaneous permeability, 10^{-3} μm^2
K_0	Initial permeability, 10^{-3} μm^2
K_c	Solubility product constant of precipitation reaction
K_d	Instantaneous permeability damage rate, dimensionless
κ	Inverse Debye length (κ^{-1} corresponds to the double-layer thickness, i.e., Debye length)
λ	Clay swelling coefficient
μ	Fluid viscosity, mPa·s
μ_s	Mean pore throat radius of the formation, μm
μ_{so}	Mean particle radius of solid phase in invading fluid, μm
η	Single collector efficiency
η_s	Ideal particle capture efficiency
φ	Porosity, %
φ_0	Initial porosity, %
ψ	Membrane exchange coefficient
P	Fluid pressure, MPa
$R_i(C)$	Characteristic reaction or retention behavior of mechanism *i*
$\boldsymbol{r}$	Spatial vector, $\boldsymbol{r} = (x, y, z)$
r_c	Critical particle radius, μm
r_m	Average pore throat diameter of porous medium, μm
r_{min}, r_{max}	Minimum/maximum pore radius of medium, μm
r_w	Wellbore radius, m
r_o	Pore throat radius of reservoir, μm
r_s	Reservoir radius, m
r_{so}	Particle radius of solid phase in invading fluid, μm
R_0	Maximum initial particle release rate
S_{ion}	Ionic strength
S_w	Water saturation, %
S_{wc}	Irreducible water saturation, %
T	Fluid temperature, K
T_{ik}	Wellbore temperature, K
T_{ck}	Reservoir temperature, K
τ	Tortuosity
θ	Corrected porosity, %
v	Actual particle–fluid velocity, m/s

u	Darcy apparent velocity of particle–fluid mixture, m/s
V	Total electrostatic potential energy
w	Mass concentration, mg/L
w_i	Effective weight of mechanism i at a given spatiotemporal point
ω_i	Precipitation coefficient of precipitate in reaction
χ	Lift coefficient
ξ_i	Volume fraction of capillary i
ρ_p	Particle density, kg/m^3
ρ_L	Fluid density, kg/m^3
ρ_s	Critical particle density, kg/m^3
σ_s	Standard deviation of formation pore throat radius, μm
σ_so	Standard deviation of particle radius in invading fluid, μm
ζ_p, ζ_g	ζ-potentials of suspended particles and matrix particles, respectively
$N(r;\, \mu_\mathrm{s}, \sigma_\mathrm{s})$	Reservoir pore size distribution function
$N_\mathrm{s}(r_\mathrm{so};\, \mu_\mathrm{so}, \sigma_\mathrm{so})$	Particle size distribution function of invading fluid solids

Appendix A. Derivation of analytical solution for diffusion–finite boundary reaction problem

A.1 Similar variable transformation

Introduce similar variables:

$$\eta_\mathrm{A} = \frac{z}{2\sqrt{Dt}} \tag{A.1}$$

Substitute variables into Eq. (26):

$$\theta_\mathrm{A}(z,t) = c(z,t) - c_0 \Rightarrow \theta(\eta_\mathrm{A}) = \Theta(\eta_\mathrm{A}) \tag{A.2}$$

The original problem is transformed into an ordinary differential equation in terms of $\Theta(\eta_\mathrm{A})$. Using the chain rule:

$$\frac{\partial \theta_\mathrm{A}}{\partial t} = -\frac{\eta_\mathrm{A}}{t}\cdot\Theta'(\eta_\mathrm{A}), \frac{\partial^2 \theta_\mathrm{A}}{\partial z^2} = \frac{1}{4Dt}\cdot\Theta''(\eta_\mathrm{A})$$

Substituting into Eq. (26) yields:

$$-\frac{\eta_\mathrm{A}}{t}\cdot\Theta' = \frac{D}{4Dt}\cdot\Theta'' \Rightarrow \Theta'' + 2\eta_\mathrm{A}\Theta' = 0 \tag{A.3}$$

A.2 Solution to the ordinary differential equation

Integrating Eq. (A.3) twice, let $\Theta' = f(\eta_\mathrm{A})$, then:

$$\frac{\mathrm{d}f}{\mathrm{d}\eta_\mathrm{A}} + 2\eta_\mathrm{A} f = 0 \Rightarrow f = C_1 \mathrm{e}^{-\eta_\mathrm{A}^2} \Rightarrow \Theta(\eta_\mathrm{A}) = C_1 \int \mathrm{e}^{-\eta_\mathrm{A}^2} \mathrm{d}\eta_\mathrm{A} + C_2 \tag{A.4}$$

The general solution is given by:

$$\theta_\mathrm{A}(z,t) = A\cdot\frac{2}{\sqrt{\pi}} \int_{\frac{z}{2\sqrt{Dt}}+B}^{\infty} \mathrm{e}^{-x^2} \mathrm{d}x \tag{A.5}$$

where B is the constant of integration.

A.3 Application of boundary conditions

Substitute Eq. (A.5) into the boundary conditions of Eq. (26) and compute the derivative:

$$\frac{\partial \theta_\mathrm{A}}{\partial z} = A\left(-\frac{1}{\sqrt{\pi Dt}} \mathrm{e}^{-\left(\frac{z}{2\sqrt{Dt}}+B\right)^2} \right) \tag{A.6}$$

Let $z = 0$ and substitute into Eq. (26) to obtain:

$$\frac{DA}{\sqrt{\pi Dt}} \mathrm{e}^{-B^2} = \psi\left(c_1 - c_0 - A\frac{2}{\sqrt{\pi}} \int_B^{\infty} \mathrm{e}^{-x^2} \mathrm{d}x \right) \tag{A.7}$$

Solving Eq. (A.7) gives the value of B, which in practical applications can be taken as:

$$B = \frac{\psi\sqrt{t}}{\sqrt{D}} \tag{A.8}$$

Substitute the above result back into the original variables to obtain the analytical solution (Eq. (27)).

Appendix B. Logarithmic coordinate transformation and derivation of difference scheme

The general form of the governing equation for damage control during the drilling and completion process is expressed as:

$$\frac{\partial C}{\partial t} + f(\vec{r},t)\nabla C(\vec{r},t) = D(\vec{r},t)\nabla^2 C(\vec{r},t) + R(C) \tag{B.1}$$

To overcome the problem of excessive grid density near the wellbore under radial coordinates, the model employs a logarithmic transformation:

$$x = \ln\left(\frac{r}{r_\mathrm{w}}\right), r = r_\mathrm{w}\mathrm{e}^x, x \in \left[0, \ln\left(\frac{r_\mathrm{max}}{r_\mathrm{w}}\right)\right] \tag{B.2}$$

By the chain rule:

$$\frac{\partial C}{\partial r} = \frac{1}{r}\frac{\partial C}{\partial x}, \frac{\partial^2 C}{\partial r^2} = \frac{1}{r^2}\left(\frac{\partial^2 C}{\partial x^2} - \frac{\partial C}{\partial x}\right) \tag{B.3}$$

Substituting Eq. (B.3) into Eq. (B.1), and letting $x_j = j\Delta x$, time step t^n, the semi-implicit difference scheme can be written as:

$$\frac{C_j^{n+1} - C_j^n}{\Delta t} + \frac{f_j}{r_\mathrm{w}\mathrm{e}^{x_j}}\cdot\frac{C_{j+1}^{n+1} - C_{j-1}^{n+1}}{2\Delta x} = \frac{D_j}{r_\mathrm{w}^2\mathrm{e}^{2x_j}}\left(\frac{C_{j+1}^{n+1} - 2C_j^{n+1} + C_{j-1}^{n+1}}{(\Delta x)^2} - \frac{C_{j+1}^{n+1} - C_{j-1}^{n+1}}{2\Delta x}\right) + R\left(C_j^n\right) \tag{B.4}$$

Eq. (B.4) can then be rearranged into a tridiagonal structure, which allows for iterative solution using Eq. (B.5).

$$C_j^{n+1} = \frac{1}{A_j}\left[C_j^n + B_j C_{j+1}^{n+1} + C_j C_{j-1}^{n+1}\right] \tag{B.5}$$

$$A_j = 1 + \frac{2D_j\Delta t}{\varphi(\Delta x)^2}$$

$$B_j = \frac{D_j\Delta t}{(\Delta x)^2} - \frac{f_j\Delta t}{2\Delta x}$$

$$C_j = \frac{D_j\Delta t}{(\Delta x)^2} + \frac{f_j\Delta t}{2\Delta x}$$

Appendix C. Input parameters for field cases

Table C.1
Input cases in Section 6

Parameter	GO7 value	YL8 value	Parameter	GO7 value	YL8 value
Engineering stage	Completion	Drilling	Clay content	15%	13%
Soaking time of invading fluid	3 d	18 d	Bound water saturation	50.1%	49.9%
Bottomhole pressure	9.5 MPa	29.473 MPa	Reservoir fluid Ca^{2+} concentration	158 mg/L	29 mg/L
Wellbore radius	0.24 m	0.09 m	Reservoir fluid Mg^{2+} concentration	27 mg/L	6 mg/L
Well deviation angle	90°	15°	Reservoir fluid Sr^{2+} concentration	/	/
Fluid loss rate	0.4 m^3/h	5 m^3/h	Reservoir fluid Ba^{2+} concentration	/	/
Viscosity of invading fluid	0.5 mPa s	60 mPa s	Reservoir fluid HCO_3^- concentration	4645 mg/L	1299 mg/L
Solid mass fraction in invading fluid	3.8%	18.48%	Reservoir fluid SO_4^{2-} concentration	26.4 mg/L	420 mg/L
Solid particle density in invading fluid	<200 mg/L	1400 mg/L	Reservoir fluid Cl^- concentration	4458 mg/L	5679 mg/L
Mean particle radius in invading fluid	<1 μm	44 μm	Invading fluid Ca^{2+} concentration	94.1 mg/L	49.7 mg/L
Std. deviation of particle radius in invading fluid	<0.5 μm	8 μm	Invading fluid Mg^{2+} concentration	127.9 mg/L	31.85 mg/L
Original reservoir pressure	22 MPa	33 MPa	Invading fluid Sr^{2+} concentration	9.3 mg/L	18.9 mg/L
Initial reservoir permeability	63×10^{-3} μm^2	88×10^{-3} μm^2	Invading fluid Ba^{2+} concentration	1.6 mg/L	6.8 mg/L
Reservoir temperature	95 °C	130 °C	Invading fluid HCO_3^- concentration	18.4 mg/L	8076 mg/L
Reservoir depth	1584.39 m	3487.48 m	Invading fluid SO_4^{2-} concentration	336.4 mg/L	6600.76 mg/L
Reservoir porosity	23%	18%	Invading fluid Cl^- concentration	2025 mg/L	30831.93 mg/L
Average pore-throat radius	6 μm	18.14 μm	Skin factor	14.76	

References

Abelson, P.H., 1973. Energy Independence. Science (New York, NY) 182 (4114), 779. https://doi.org/10.1126/science.182.4114.779.

Azizi, J., Shadizadeh, S.R., Manshad, A.K., 2019. A dynamic method for experimental assessment of scale inhibitor efficiency in oil recovery process by water flooding. Petroleum 5, 303–314. https://doi.org/10.1016/j.petlm.2018.07.004.

Bui, D., Nguyen, T., Nguyen, Th, et al., 2023. Formation damage simulation of a multi-fractured horizontal well in a tight gas/shale oil formation. J. Pet. Explor. Prod. Technol. 13 (1), 163–184. https://doi.org/10.1007/s13202-022-01544-8.

Cao, J., Zhang, N., Johansen, T.E., 2019. Applications of fully coupled well/near-well modeling to reservoir heterogeneity and formation damage effects. J. Petrol. Sci. Eng. 176, 640–652. https://doi.org/10.1016/j.petrol.2019.01.091.

Cho, J., Min, B., Kwon, S., et al., 2021. Compositional modeling with formation damage to investigate the effects of CO_2-CH_4 water alternating gas (WAG) on performance of coupled enhanced oil recovery and geological carbon storage. J. Petrol. Sci. Eng. 205, 108795. https://doi.org/10.1016/j.petrol.2021.108795.

Civan, F., 2007. Reservoir Formation Damage: Fundamentals, Modeling, Assessment, and Mitigation. Gulf Professional Publishing, Elsevier, USA.

Cui, G., Ning, F., Dou, B., et al., 2022. Particle migration and formation damage during geothermal exploitation from weakly consolidated sandstone reservoirs via water and CO_2 recycling. Energy 240, 122507. https://doi.org/10.1016/j.energy.2021.122507.

Davarpanah, A., Mirshekari, B., Razmjoo, A., 2020. A parametric study to numerically analyze the formation damage effect. Energy Explor. Exploit. 38 (2), 555–568. https://doi.org/10.1177/0144598719873094.

Ding, D.Y., 2011. Coupled simulation of near-wellbore and reservoir models. J. Petrol. Sci. Eng. 76 (1–2), 21–36. https://doi.org/10.1016/j.petrol.2010.12.004.

Elimelech, M., Gregory, J., Jia, X., et al., 1995. Particle Deposition and Aggregation. Butterworth-Heinemann, Boston. https://doi.org/10.1016/C2013-0-04548-3.

Han, X.D., Zhong, L.G., Liu, Y.G., et al., 2020. Experimental study and pore network modeling of formation damage induced by fines migration in unconsolidated sandstone reservoirs. Journal of Energy Resources Technology-Transactions of the Asme 142 (11), 113006. https://doi.org/10.1115/1.4047594.

Jiang, G., Sheng, K., He, Y., et al., 2024. Numerical simulation of the temporal and spatial evolution of sandstone pore type reservoir damage types and severity. Sci. Rep. 14, 25401. https://doi.org/10.1038/s41598-024-76383-0.

Jiang, G., Sun, Z., Sheng, K., et al., 2022. A quantitative simulation method for temporal and spatial evolution of bacterial plugging in sandstone reservoirs during water-flooding. Journal of China University of Petroleum (Edition of Natural Science) 46 (6), 110–118. https://doi.org/10.3969/j.issn.1673-5005.2022.06.012 (in Chinese).

Jin, L., Zeng, Y., Cheng, T., et al., 2021. Seepage clogging characteristics of rock and soil porous media using LBM-IMB-DEM simulation method. Chin. J. Geotech. Eng. 43 (5), 909–917. https://doi.org/10.11779/CJGE202105015.

Kargozarfard, Z., Haghtalab, A., Ayatollahi, S., 2023. A nanoscale insight into the formation damage of carbonate reservoir due to water incompatibility during smart water injection: A molecular dynamics study. Computational Particle Mechanics 10 (4), 887–910. https://doi.org/10.1007/s40571-022-00534-1.

Khilar, K.C., Fogler, S., 1998. Migration of Fines in Porous Media. Kluwer Academic Publishers, Dordrecht. https://doi.org/10.1007/978-94-015-9074-7.

Khormali, A., Petrakov, D., Moein, M., 2016. Experimental analysis of calcium carbonate scale formation and inhibition in waterflooding of carbonate reservoirs. J. Petrol. Sci. Eng. 147, 843–850. https://doi.org/10.1016/j.petrol.2016.09.048.

Li, J., Xiong, G., Li, N., et al., 2023. Simulation of sandstone formation damage caused by solid particle invasion. J. Dispersion Sci. Technol. 45 (9), 1767–1778. https://doi.org/10.1080/01932691.2023.2229899.

Li, Y., Jiang, G., Li, X., et al., 2022. Quantitative investigation of water sensitivity and water locking damages on a low-permeability reservoir using the core flooding experiment and NMR test. ACS Omega 7 (5), 4444–4456. https://doi.org/10.1021/acsomega.1c06293.

Ma, T., Peng, N., Chen, P., 2020. Filter cake formation process by involving the influence of solid particle size distribution in drilling fluids. J. Nat. Gas Sci. Eng. 79, 103350. https://doi.org/10.1016/j.jngse.2020.103350.

Ngata, M.R., Yang, B.L., Khalid, W., et al., 2023. Review on experimental investigation into formation damage during geologic carbon sequestration: Advances and outlook. Energy Fuels 37 (9), 6382–6400. https://doi.org/10.1021/acs.energyfuels.3c00427.

Oddo, J.E., Tomson, M., 1994. Why scale forms and how to predict it. SPE Prod. Facil. 47–54. https://doi.org/10.2118/21710-PA.

Ott, H., Bakel, M., Vos, F., et al., 2012. Core-flood experiment for transport of reactive fluids in rocks. Rev. Sci. Instrum. 83, 084501. https://doi.org/10.1063/1.4746997.

Peng, N., Ma, T., Chen, P., 2021. Fully coupled thermal-hydro-mechanical model of pore pressure propagation around borehole with dynamic mudcake growth. J. Nat. Gas Sci. Eng. 96, 104330. https://doi.org/10.1016/j.jngse.2021.104330.

Peng, N., Ma, T., Xu, H., et al., 2025. Numerical modeling for drilling fluid invasion in a coupled wellbore–formation system. Phys. Fluids 37, 096606. https://doi.org/10.1063/5.0289162.

Rabczuk, T., Belytschko, T., 2004. Cracking particles: A simplified meshfree method for arbitrary evolving cracks. Int. J. Numer. Methods Eng. 61 (13), 2316–2343. https://doi.org/10.1002/nme.1151.

Rezaeizadeh, M., Hajiabadi, S.H., Aghaei, H., et al., 2021. Pore-scale analysis of formation damage; A review of existing digital and analytical approaches. Adv. Colloid Interface Sci. 288, 102345. https://doi.org/10.1016/j.cis.2020.102345.

Sheng, K., Jiang, G., 2023. Prediction of four kinds of sensibility damages to hydrocarbon reservoirs based on random forest algorithm. Drilling & Completion Fluid 40 (4), 423–430. https://doi.org/10.12358/j.issn.1001-5620.2023.04.002.

Wang, T., Guo, Z., Li, G., et al., 2023. Numerical simulation of three-dimensional fracturing fracture propagation in radial wells. Petrol. Explor. Dev. 50 (3), 613–623. https://doi.org/10.1016/S1876-3804(23)60421-5.

Wen, Z., Wang, J., Wang, Z., et al., 2023. Analysis of the world deepwater oil and gas exploration situation. Petrol. Explor. Dev. 50 (5), 1060–1076. https://doi.org/10.1016/S1876-3804(23)60449-5.

Wu, J.C., Fan, Y.R., Wu, F., et al., 2019. Combining large-sized model flow experiment and NMR measurement to investigate drilling induced formation damage in sandstone reservoir. J. Petrol. Sci. Eng. 176, 85–96. https://doi.org/10.1016/j.petrol.2019.01.005.

Xiong, Z., Wang, G.Q., Zhang, Y.G., et al., 2022. Application of digital rock technology for formation damage evaluation in tight sandstone reservoir. J. Pet. Explor. Prod. Technol. 13, 803–812. https://doi.org/10.1007/s13202-022-01576-0.

Xu, J., 2019. Numerical Simulation of multi-factor Reservoir Damage. Master's Thesis. China University of Petroleum (Beijing), Beijing.

Xu, J., Jiang, G., 2018. Time-fractional characterization of brine reaction and precipitation in porous media. Phys. Rev. 97, 042133. https://doi.org/10.1103/PhysRevE.97.042133.

Yang, Y., Siqueira, F.D., Vaz, A.S.L., et al., 2016. Slow migration of detached fine particles over rock surface in porous media. J. Nat. Gas Sci. Eng. 34, 1159–1173. https://doi.org/10.1016/j.jngse.2016.07.056.

Zhou, N., Lu, S., Zhang, P., et al., 2023. Tight gas charging and accumulation mechanisms and mathematical model. Petrol. Explor. Dev. 50 (6), 1233–1244. https://doi.org/10.1016/S1876-3804(24)60476-3.

Zou, C., Pan, S., Zhao, Q., 2020. On the connotation, challenge and significance of China's "energy independence" strategy. Petrol. Explor. Dev. 47 (2), 416–426. https://doi.org/10.1016/S1876-3804(20)60062-3.